Intermittency in Collisionless Large-Amplitude Turbulence

Ryan Golant , ¹ Luca Comisso , ¹ Philipp Kempski , ¹ and Lorenzo Sironi , ¹

¹Department of Astronomy and Columbia Astrophysics Laboratory, Columbia University, New York, NY, 10027, USA

²Center for Computational Astrophysics, Flatiron Institute, 162 5th Avenue, New York, NY 10010, USA

(Received November 7, 2025)

Submitted to ApJ

ABSTRACT

Large-amplitude turbulence – characterized by a fluctuating magnetic field component, δB , that is stronger than the mean component, B_0 – is generically intermittent, populated with intense localized structures such as sharp field-line bends and rapid field reversals. Recent MHD simulations suggest that these structures play an important role in particle transport and acceleration; however, MHD is inapplicable in most of our Universe, where the plasma is so hot or diffuse that Coulomb collisions are negligible. Therefore, in this paper, we analyze the intermittent properties of collisionless large-amplitude turbulence in electron-positron plasmas via fully kinetic 3D simulations, exploring a wide range of $\delta B/B_0$ and scale separations between the turbulence driving scale, L, and kinetic scales, c/ω_p . The steady-state collisionless turbulence in our simulations broadly resembles that of MHD, but the development of pressure anisotropy steepens the scaling between magnetic field strength, B, and scalar field-line curvature, B_\parallel – yielding $B_\parallel \propto K_\parallel^{-3/4}$ – and consequently modifies the power-law slope of the probability density function of B_\parallel ; this slope hardens from B_\parallel 0 to B_\parallel 1 as B_\parallel 2 increases from 4 to 140. Pressure anisotropy also triggers mirror and firehose instabilities, with the volume-filling fractions of these fluctuations increasing with B_\parallel 2 for our largest B_\parallel 3. 20% of the volume is mirror-unstable and 6% is firehose-unstable. Both the curvature and the Larmor-scale fluctuations in collisionless large-amplitude turbulence are expected to significantly influence cosmic ray transport and acceleration in the interstellar medium of our Galaxy and the intracluster medium of galaxy clusters.

Keywords: Magnetic fields (994) — Extragalactic magnetic fields (507) —Milky Way magnetic fields (1057) — Plasma astrophysics (1261) — Cosmic rays (329)

1. INTRODUCTION

A wide array of astrophysical systems – from planetary and stellar interiors to powerful accretion flows and winds to the interstellar and intracluster media – exist in a state of magnetized turbulence (D. Biskamp 2003; A. A. Schekochihin & S. C. Cowley 2007; P. A. Davidson 2015). In this state, the chaotic advection, stretching, and folding of the magnetic field by turbulent motions is balanced by the back-reaction of the magnetic field via the Lorentz force. This nonlinear interplay between the velocity and magnetic fields dictates the morphology of the magnetic field and the shape of the magnetic power spectrum (P. Goldreich & S. Sridhar 1995;

Email: ryan.golant@columbia.edu

J. Cho & A. Lazarian 2003; A. A. Schekochihin et al. 2004; S. Boldyrev 2006; A. Beresnyak 2019; J. R. Beattie et al. 2025), the nature of cross-scale energy transfer and the details of small-scale dissipation (E. Quataert & A. Gruzinov 1999), and the efficacy of heat (R. Narayan & M. V. Medvedev 2001; T. J. Dennis & B. D. G. Chandran 2005), angular momentum (N. I. Shakura & R. A. Sunyaev 1973; S. A. Balbus & J. F. Hawley 1998), and particle transport (E. G. Zweibel 2013, 2017; A. Lazarian et al. 2023). As such, a comprehensive understanding of magnetized turbulence is a prerequisite to understanding much of our Universe. Unfortunately, a complete, unified theory of magnetized turbulence still eludes us (A. A. Schekochihin 2022).

One impediment to a complete theory of magnetized turbulence is our hazy understanding of intermittency,

or the presence of sparse, intense, coherent structures such as current sheets, plasmoids, and sharp magnetic field-line bends – arising from spatio-temporal nonuniformity in the turbulent energy cascade (W. H. Matthaeus et al. 2015; L. Vlahos & H. Isliker 2023; T. Ha et al. 2025). Previous studies show that these intermittent structures can modulate how energy is dissipated (M. Wan et al. 2012; V. Zhdankin et al. 2013; M. Zhou et al. 2023; Z. Davis et al. 2024), how magnetic fields are amplified (A. K. Galishnikova et al. 2022; L. Sironi et al. 2023; M. Zhou et al. 2024; J. R. Beattie et al. 2024), and how particles are scattered (D. B. Fielding et al. 2023; P. Kempski et al. 2023; M. Lemoine 2023) and accelerated (L. Comisso & L. Sironi 2018, 2019, 2022; J. Nättilä 2024; M. Lemoine 2025). Detrimentally, however, intermittency is absent from quasilinear models that treat turbulence as a sum of linear plane waves with uncorrelated random phases (J. Maron & P. Goldreich 2001). Furthermore, because intermittent structures form prominently non-Gaussian distributions, they cannot be properly captured by two-point statistics like the power spectrum (Z.-S. She & E. Leveque 1994). Therefore, careful analysis of numerical simulations that go beyond simplistic synthetic wave turbulence is necessary to diagnose the impact of intermittency on magnetized turbulence.

Recently, intermittency in the regime of largeamplitude magnetohydrodynamic (MHD) turbulence has received increased attention for its potential role in Galactic cosmic ray transport (M. Lemoine 2023; P. Kempski et al. 2023, 2025; I. S. Butsky et al. 2024; J. Lübke et al. 2025). This regime is characterized by a fluctuating magnetic field component, δB , that exceeds the mean component, B_0 , due to the turbulent amplification of an initially weak field (A. A. Schekochihin et al. 2004). In contrast to turbulence with $\delta B/B_0 \lesssim 1$, the magnetic field lines in large-amplitude turbulence are tangled and bent nearly isotropically (or fully isotropically in the $\delta B/B_0 \to \infty$ case, corresponding to the saturated state of the small-scale dynamo) (A. A. Schekochihin & S. C. Cowley 2007). The curvature of these field-line bends forms a wide power-law distribution cutting off near the resistive scale; this distribution has been hypothesized to make the transport of particles through the turbulence energy-dependent, since particles with smaller gyroradii can stay attached to field lines with tighter bends (P. Kempski et al. 2023; M. Lemoine 2023). MHD simulations show that the geometry of the magnetic field and the transport of cosmic rays in large-amplitude turbulence are sensitive to both $\delta B/B_0$ and the numerical grid resolution, but the detailed effects of these variables require further study (P. Kempski et al. 2025).

Crucially, however, the aforementioned picture of intermittency in large-amplitude MHD turbulence may break down in hot and low-density astrophysical environments where the mean free path to Coulomb collisions is large compared to the dynamical scales of interest; in such weakly collisional or collisionless environments, which include the intracluster medium and the hot interstellar medium, the collisional MHD description is no longer accurate and we must consider kinetic effects (M. W. Kunz et al. 2022). For instance, turbulent, magnetized, collisionless plasmas readily develop pressure anisotropy due to the conservation of particle magnetic moments (or, equivalently, conservation of the CGL invariants; G. F. Chew et al. (1956)): the pressure perpendicular to the magnetic field (P_{\perp}) exceeds the parallel pressure (P_{\parallel}) where the turbulent motions strengthen the field, while the parallel pressure dominates where the field is weakened.

If the plasma β – the ratio of the thermal pressure to the magnetic pressure – is high, then pressure anisotropy can trigger kinetic instabilities in collisionless plasmas (L. Arzamasskiy et al. 2023). Such instabilities include the mirror (A. Barnes 1966; A. Hasegawa 1969) and firehose (M. N. Rosenbluth 1956; S. Chandrasekhar et al. 1958; E. N. Parker 1958) instabilities, which grow preferentially on thermal Larmor scales and grow rapidly compared to fluid-scale flows, allowing these instabilities to significantly modify the turbulence (S. P. Gary 1993; L. Arzamasskiy et al. 2023). In regions where $P_{\perp}/P_{\parallel} > 1 + 1/\beta$, the mirror instability causes field lines to bubble up, producing microscopic magnetic mirrors (F. Rincon et al. 2015); in regions where $P_{\perp}/P_{\parallel} \lesssim$ $1-2/\beta$, the firehose instability causes Alfvén waves to grow exponentially, relaxing field-line tension (C.-S. Jao & L.-N. Hau 2020). Not only do these instabilities alter the local geometry of the magnetic field, they can also suppress field-strength variations and anisotropic pressure stresses and introduce non-local energy transfer, ultimately changing the material properties of the plasma (J. Squire et al. 2019, 2023; S. Majeski et al. 2024). Given these kinetic effects, collisionless largeamplitude turbulence may look much different from its MHD counterpart.

Some initial insight into the general nature of collisionless large-amplitude turbulence can be gained by looking at previous simulations of the collisionless small-scale dynamo, the extreme $(\delta B/B_0 \to \infty)$ limit of this regime (F. Rincon et al. 2016; D. A. St-Onge & M. W. Kunz 2018; L. Sironi et al. 2023; M. Zhou et al. 2024; R. Achikanath Chirakkara et al. 2024). In these simula-

tions, mirror and firehose instabilities are triggered during the kinematic dynamo phase – when the magnetic field is still too weak to affect the flow – seeding small-scale magnetic fluctuations that provide an effective collisionality for the particles. Hence, even in the absence of Coulomb collisions, the plasma develops fluid-like behavior. In saturation, the magnetic field forms a large-scale folded sheet structure reminiscent of the equivalent MHD dynamo (A. A. Schekochihin et al. 2004); on small scales, however, the magnetic field is locally corrugated by nonlinear mirrors and firehoses. Whether this same general agreement with MHD holds at smaller $\delta B/B_0 > 1$ is a central focus of this work.

In this paper, we analyze the intermittent properties of moderately subsonic, large-amplitude turbulence in a collisionless electron-positron plasma via an extensive suite of fully kinetic 3D simulations covering a wide range of $\delta B/B_0$ (from $\delta B/B_0 \approx 1$ up to $\delta B/B_0 \approx 140$) and of scale separation between the turbulent driving scale and kinetic scales (using simulation boxes with $L/(c/\omega_{\rm p}) = \{500, 1000, 2000\}, \text{ for } c/\omega_{\rm p} \text{ the plasma skin}$ depth and L the box size, which is also our driving scale). We primarily focus on the statistics of magnetic fieldline curvature – which has direct connections to particle transport and acceleration (e.g., P. Kempski et al. (2023, 2025); M. Lemoine (2025)) – probing how kinetic effects yield deviations from MHD. Broadly, the steady-state turbulence in our collisionless simulations resembles that of MHD, as had previously been seen in the case of the collisionless small-scale dynamo. However, the development of pressure anisotropy steepens the scaling between magnetic field strength and scalar field-line curvature and consequently modifies the power-law slope of the probability density function of curvature. Pressure anisotropy also triggers mirror and firehose instabilities in each of our simulations, with the volume-filling fractions of these fluctuations increasing with $\delta B/B_0$. Both the curvature and the Larmor-scale fluctuations in collisionless large-amplitude turbulence are expected to significantly influence cosmic ray transport and acceleration in $\beta \gtrsim 1$ plasmas such as the hot interstellar medium of our Galaxy and the intracluster medium of galaxy clusters.

This paper is structured as follows: in Section 2 we detail the setup of our simulation suite; in Section 3 we provide an overview of the salient properties of the steady-state turbulence in our simulations; in Section 4 we analyze the statistics of magnetic field-line curvature; in Section 5 we show how pressure anisotropy modifies the curvature statistics; in Section 6 we connect our results to particle transport and acceleration;

and in Section 7 we summarize our main results and conclude.

2. SIMULATION SETUP

We run fully periodic 3D simulations of moderately subsonic, large-amplitude turbulence in a collisionless electron-positron plasma using the electromagnetic particle-in-cell (PIC) code TRISTAN-MP (H. Matsumoto & Y. Omura 1993; A. Spitkovsky et al. 2019). The code solves the Maxwell-Vlasov system using a second-order Finite-Difference Time-Domain (FDTD) scheme on a standard Yee mesh (K. Yee 1966) and pushes particles using the Boris algorithm (J. P. Boris 1970) and first-order shape functions. The electromagnetic fields are extrapolated to the particle positions using a trilinear interpolation function. At each time step, after depositing the electric current to the grid using the charge-conserving zig-zag scheme (T. Umeda et al. 2003), we apply ten passes of a 3-point (1-2-1) digital current filter in each direction to smooth out nonphysical short-wavelength oscillations. The simulations analyzed in the main text use 8 particles per cell per species and a grid resolution of 1 plasma skin depth, $c/\omega_{\rm p} \equiv \left(m_{\rm e}c^2/4\pi n_0e^2\right)^{1/2}$, where n_0 is the uniform initial density of the plasma (including both species) and c is the speed of light, set to 0.45 cells per timestep.

To drive turbulence, we add a charge-independent external acceleration term, $\mathbf{a}(\mathbf{x},t)$, to the particle equations of motion (L. Sironi et al. 2023). This acceleration field is decomposed into six independently evolving Fourier modes such that

$$\mathbf{a}(\mathbf{x},t) = \Re \left[\sum_{\mathbf{k}} \tilde{\mathbf{a}}(\mathbf{k},t) e^{i\mathbf{k}\cdot\mathbf{x}} \right],\tag{1}$$

where the sum is over all six modes, each driven at the simulation box scale, L: $\mathbf{k}L/2\pi = \{(\pm 1,0,0),(0,\pm 1,0),(0,0,\pm 1)\}$. $\tilde{\mathbf{a}}(\mathbf{k},t)$ in Equation (1) is the amplitude of mode \mathbf{k} , advanced in Fourier space according to an Ornstein-Uhlenbeck process (G. E. Uhlenbeck & L. S. Ornstein 1930; J. Zrake & A. I. MacFadyen 2012):

$$d\tilde{\mathbf{a}}(\mathbf{k},t) = -\gamma_{\text{corr}}\tilde{\mathbf{a}}(\mathbf{k},t)dt + \sqrt{\gamma_{\text{corr}}P_k}\mathbf{T}(\mathbf{k}) \cdot d\tilde{\mathbf{W}}(\mathbf{k},t).$$
(2)

The first term on the right-hand side of this equation functions as a "drag" term pulling $\tilde{\mathbf{a}}(\mathbf{k},t)$ towards its mean, with the efficacy of this drag set by the decorrelation rate $\gamma_{\rm corr} \simeq 1.5/t_{\rm L}$ (for $t_{\rm L}$ the turnover time); this drag modulates the Wiener process (i.e., the continuous random walk) modeled by the second term on the right-hand side. In this second term, $d\tilde{\mathbf{W}}(\mathbf{k},t)$ is a complex random variable with real and imaginary parts each

uniformly distributed within [-1/2, 1/2], while $\mathbf{T}(\mathbf{k})$ is a projection operator that dictates the fraction of each driven mode that goes into compressive vs. shearing/solenoidal motions,

$$\mathbf{T}(\mathbf{k}) \equiv (1 - \zeta)\mathbf{T}_{\parallel}(\mathbf{k}) + \zeta\mathbf{T}_{\perp}(\mathbf{k}), \tag{3}$$

where

$$\mathbf{T}_{\parallel}(\mathbf{k}) \cdot d\tilde{\mathbf{W}}(\mathbf{k}, t) = \left[\hat{\mathbf{k}} \cdot \tilde{\mathbf{W}}(\mathbf{k}, t)\right] \hat{\mathbf{k}}$$
(4)

and

$$\mathbf{T}_{\perp}(\mathbf{k}) \cdot d\tilde{\mathbf{W}}(\mathbf{k}, t) = d\tilde{\mathbf{W}} - \left[\hat{\mathbf{k}} \cdot \tilde{\mathbf{W}}(\mathbf{k}, t)\right].$$
 (5)

In Equation 3, $\zeta=0$ corresponds to purely compressive driving and $\zeta=1$ corresponds to purely solenoidal driving. All of the simulations analyzed in this paper use purely solenoidal driving. ³ The factor P_k in Equation (2), which is the same for all modes, serves as a normalization accounting for the different degrees of freedom in compressive vs. solenoidal modes; more precisely, $P_k \propto \left[(1-\zeta)^2 + 2\zeta^2 \right]^{-1}$, where the constant of proportionality sets the target root-mean-squared velocity of the turbulent driver, $u_{\rm rms,0}$.

We choose numerical parameters such that the turbulent driver produces a non-relativistic and moderately subsonic flow. The plasma is initialized from a Maxwellian distribution with $k_{\rm B}T_0/m_{\rm e}c^2=0.04$, where T_0 is the initial temperature of both the electrons and the positrons; this implies a thermal speed of $v_{\rm th} \equiv$ $\sqrt{2k_BT_0/m_e} \approx 0.3c$. The plasma temperature remains roughly constant due to our particle cooling prescription: to keep the system in quasi-steady state, we artificially cool particles that exceed a threshold momentum of $p_{\rm cut}/m_{\rm e}c = 0.7$, resetting the momentum to $p_{\rm cut}$ and keeping the particle's direction unchanged. By setting the target rms velocity of our driver to $u_{\rm rms,0} = 0.2c$, the sonic Mach number of the turbulence oscillates around a steady value, $M_{\rm s} \equiv u_{\rm rms}/v_{\rm th} \approx 0.7$ (or $u_{\rm rms}/c_s \approx 0.8$ for $c_s \equiv \sqrt{(5/3)k_BT_0/m_e}$, where $u_{\rm rms}$ is the instantaneous rms velocity of the flow; therefore, our turbulence remains moderately subsonic for the majority of its time-evolution (see Figure 1). By normalizing the Mach number to $v_{\rm th}$ (which is standard in the collisionless dynamo literature, e.g., F. Rincon et al. (2016); D. A. St-Onge & M. W. Kunz (2018); M. Zhou et al. (2024); R. Achikanath Chirakkara et al. (2024)), M^2 yields a measurement of the ratio of turbulent kinetic energy to thermal energy:

$$M_{\rm s}^2 = \frac{\frac{1}{2} m_e u_{\rm rms}^2}{k_{\rm B} T_0}.$$
 (6)

The key physical parameters that we vary throughout our simulation suite are the initial mean magnetic field strength, B_0 , and the scale separation between the driving scale and kinetic scales, $L/(c/\omega_p)$, set by the simulation box size, L. We initialize each simulation with a seed magnetic field pointing in the z direction with strength set by the initial inverse plasma β ,

$$\beta_0^{-1} \equiv \frac{B_0^2}{8\pi n_0 k_{\rm B} T_0}. (7)$$

We evolve our simulations until the magnetic field amplification saturates and the turbulence reaches a steady state, as illustrated in Figure 1. In steady state, we quantify the strength of the turbulence via the ratio of the rms strength of the fluctuating component of the magnetic field to the strength of the mean field,

$$\frac{\delta B}{B_0} \equiv \frac{\sqrt{\langle \delta B^2 \rangle}}{B_0},\tag{8}$$

where angled brackets indicate averaging over the whole volume. Throughout this paper, we use $\delta B/B_0$ to label our simulations; in Table 1, we show the correspondence between our input mean-field strengths (i.e, β_0^{-1}), the measured (time-averaged) $\delta B/B_0$ in steady-state, and the measured (time- and spatial-averaged) plasma β in steady state, computed as

$$\beta \equiv \frac{8\pi n_0 k_{\rm B} T_0}{\langle B^2 \rangle},\tag{9}$$

for B the local magnetic field strength. Coupled with Equation (6), $M_{\rm s}^2 \beta \sim 1$ provides a convenient condition for energy equipartition.

For each $\delta B/B_0$, we run three simulations with boxes of size $L^3 = (500\,c/\omega_{\rm p})^3$, $(1000\,c/\omega_{\rm p})^3$, and $(2000\,c/\omega_{\rm p})^3$ to check the dependence of the turbulence on scale separation between the driving scale and kinetic scales, $L/(c/\omega_{\rm p})$. Unless otherwise noted, the data shown in the main text of this paper correspond to our largest (i.e., $(2000\,c/\omega_{\rm p})^3)$ boxes.

To smooth out statistical fluctuations in our measurements of the turbulence, we average our results over at least five snapshots in steady state, each spaced $9\,t_{\rm L}$ apart; all of the figures in this paper (except for the time series and simulation-box visualizations) show time-averaged quantities. Additionally, to ensure that our measurements of intermittency are not affected by

³ While compressive modes may be important for particle acceleration (e.g., V. Zhdankin (2021); G. Brunetti & A. Lazarian (2007)), previous simulations of MHD turbulence suggest that these modes have a subdominant impact on particle transport, accounting for only a small fraction of the turbulent kinetic energy (P. Kempski et al. 2023; Z. Gan et al. 2022).

β_0^{-1}	$\delta B/B_0$	β
3.75×10^{-1}	1	1.2
1.25×10^{-1}	2	1.6
3.75×10^{-2}	4	1.8
1.25×10^{-2}	6	1.8
3.75×10^{-3}	10	2.4
1.25×10^{-3}	16	3.0
1.25×10^{-4}	45	3.6
1.25×10^{-5}	140	3.5
0	∞	3.8

Table 1. Correspondence between the initial mean-field strength, β_0^{-1} (Equation (7)), the measured amplitude of the resulting steady-state turbulence, $\delta B/B_0$ (Equation (8)), and the measured steady-state plasma β (Equation (9)) for each of our simulations. The values of both $\delta B/B_0$ and β have been time-averaged across the steady-state duration.

small-scale noise – which poses a particular problem when numerically computing spatial gradients – we filter out the magnetic field at scales below $\sim 9\,c/\omega_{\rm p}$, corresponding to the scale at which the magnetic power spectrum becomes noise-dominated (see Section 3); to do this, we Fourier transform the magnetic field, set all modes with wavenumber greater than 0.7 $(c/\omega_{\rm p})^{-1}$ to 0, then inverse transform back to real space. This filtering makes our measurements of the magnetic field-line geometry more robust.

3. GENERAL PROPERTIES OF THE TURBULENCE IN STEADY STATE

Throughout this paper, we discuss the properties of our simulated turbulence in steady state. To start, therefore, it is instructive to describe the evolution of our simulations towards this steady state.

Figure 1 shows the full time-evolution of the magnetic energy (top panel) and of the kinetic energy (bottom panel) for each of our simulations with $L/(c/\omega_{\rm p}) = 2000$; darker colors correspond to larger $\delta B/B_0$. For every $\delta B/B_0$, the initial magnetic field experiences some degree of amplification that saturates within a few tens of $t_{\rm L} \equiv L/2\pi u_{\rm rms,0}$ (with the time of saturation dependent on β_0^{-1}), yielding near-equipartition between the magnetic and kinetic energies. This is the first time that turbulent magnetic field amplification has been demonstrated in fully-kinetic collisionless turbulence with a non-zero mean field; while previous work showed that the early growth of the magnetic field in the $B_0 = 0$ (i.e., $\delta B/B_0 \to \infty$) case was due purely to fields seeded by the Weibel instability (L. Sironi et al. 2023; M. Zhou et al. 2024), it remains the subject of future work to describe the role of collisionless effects at early times for larger B_0 (i.e., smaller $\delta B/B_0$). This early physics

may explain the bifurcation we see in magnetic field evolution between $\delta B/B_0 \approx 16$ and $\delta B/B_0 \approx 45$: the larger $\delta B/B_0$ cases $(\delta B/B_0 \gtrsim 45)$ grow gradually, clustering around the $\delta B/B_0 \to \infty$ case by $90\,t_{\rm L}$, while the smaller $\delta B/B_0$ cases $(\delta B/B_0 \lesssim 16)$ grow rapidly, reaching saturation by $20\,t_{\rm L}$. These two regimes are evident across a diverse array of measurements, as we shall see throughout this paper. Because the steady-state properties of the larger $\delta B/B_0$ simulations all closely resemble those of the $\delta B/B_0 \to \infty$ simulation, we discard the $\delta B/B_0 \to \infty$ case from further plots; see L. Sironi et al. (2023) for further analysis of this case.

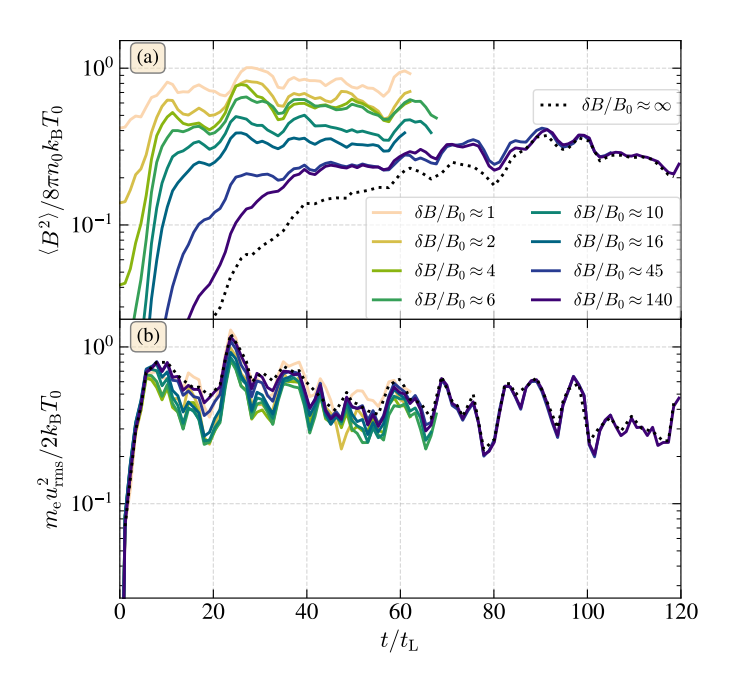


Figure 1. Time evolution of the magnetic energy (top panel) and the kinetic energy (bottom panel) for each of our simulations with $L/(c/\omega_{\rm P})=2000$; the unmagnetized dynamo case, $\delta B/B_0 \to \infty$, is depicted with a dotted curve to distinguish it from the rest of the cases. The magnetic energy is normalized to give $1/\beta$ at fixed temperature (Equation (9)) and the kinetic energy is normalized to give the square of the sonic Mach number at fixed temperature (Equation (6)). Each simulation reaches a steady state within a few tens of eddy turnover times, $t_{\rm L} \equiv L/2\pi u_{\rm rms,0}$.

The magnetic energy in Figure 1 is normalized to give $1/\beta$, for β defined in Equation (9). As illustrated in this plot and in Table 1, our simulations span a wide range of β in steady state: the smaller $\delta B/B_0$ cases reach β of order unity, characteristic of the interstellar medium of galaxies, while the larger $\delta B/B_0$ cases develop higher- β turbulence, more characteristic of the intracluster medium of galaxy clusters.

In the bottom panel of Figure 1, the kinetic energy is normalized to give the square of the sonic Mach number, $M_{\rm s}^2$, under the assumption of constant temperature, as defined in Equation (6). Evidently, the strength of the mean magnetic field has only a minor impact on the development of the turbulent flow: for every $\delta B/B_0$, the rms velocity quickly reaches a steady state (within $10\,t_{\rm L}$) that fluctuates around the target $u_{\rm rms,0}$ of 0.2c, or around $M_s\approx 0.7$. Therefore, the turbulence in each of our simulations remains moderately subsonic throughout the majority of its time-evolution. The largest Alfvén speed reached in our simulations is $v_{\rm A}\approx 0.3c$, making our turbulence safely non-relativistic.

To understand the distribution of energy as a function of spatial scale in our developed turbulence, we plot the steady-state isotropic magnetic (top panel) and kinetic (bottom panel) power spectra, M(k) and K(k), respectively, in Figure 2; the spectra are normalized such that the integral over the magnetic spectrum yields $1/\beta$ (Equation (9)) and the integral over the kinetic spectrum yields $M_{\rm s}^2$ (Equation (6)). The bifurcation between large $\delta B/B_0$ and small $\delta B/B_0$ is also evident in these spectra: the large $\delta B/B_0$ cases produce dynamo-like spectra with most of the magnetic energy residing well below the outer scale (peaking around $k c/\omega_{\rm p} \sim 0.04$), while the small $\delta B/B_0$ cases have pronounced peaks at the outer scale (due largely to the mean field), forming Kolmogorov-like spectra with slopes close to -5/3 persisting across a well-defined inertial range $(10^{-2} \lesssim k c/\omega_p \lesssim 10^{-1})$ (A. Kolmogorov 1941).

We can quantify the dominant scale of the magnetic field via the integral-scale wavenumber,

$$k_{\rm int} \equiv \frac{\int \mathbf{M}(k) \, \mathrm{d}k}{\int k^{-1} \, \mathbf{M}(k) \, \mathrm{d}k}; \tag{10}$$

while the $\delta B/B_0 \gtrsim 16$ cases each have $k_{\rm int} \, c/\omega_{\rm p} \sim 2 \times 10^{-2}$ (or a physical scale, $L_{\rm int} \equiv 2\pi/k_{\rm int}$, around one-sixth of the box scale, L), $k_{\rm int}$ steadily decreases with lower $\delta B/B_0$, reaching $k_{\rm int} \, c/\omega_{\rm p} \sim 10^{-2}$ (or $L_{\rm int} \sim L/3$) for $\delta B/B_0 \approx 1$. $L_{\rm int}$ increases linearly with box size: as shown in Figure 16, increasing $L/(c/\omega_{\rm p})$ by a factor of two decreases $k_{\rm int}$ (and increases $L_{\rm int}$) also by a factor of two.

As illustrated in the bottom panel of Figure 2, each of our simulations develops a full turbulent cascade running from the box scale down to the grid scale. The steep drop in the kinetic spectra at low k ($k c/\omega_{\rm p} \sim 0.004-0.005$) indicates that not all kinetic energy injected at the driving scale cascades to smaller scales; indeed, for all $\delta B/B_0$, the kinetic energy remains subdominant to the magnetic energy throughout the inertial range ($10^{-2} \lesssim k c/\omega_{\rm p} \lesssim 10^{-1}$). However, the kinetic spectra fall off more gradually than the mag-

netic spectra at high $k~(k\,c/\omega_{\rm p}\gtrsim 10^{-1})$; the kinetic spectra steepen mildly as they enter a dissipative range around $k\,c/\omega_{\rm p}\sim 3\times 10^{-1}$, while the magnetic spectra steepen dramatically beyond $k\,c/\omega_{\rm p}\sim 2\times 10^{-1}$, with this magnetic dissipative cutoff shifting towards higher k for larger $\delta B/B_0$.

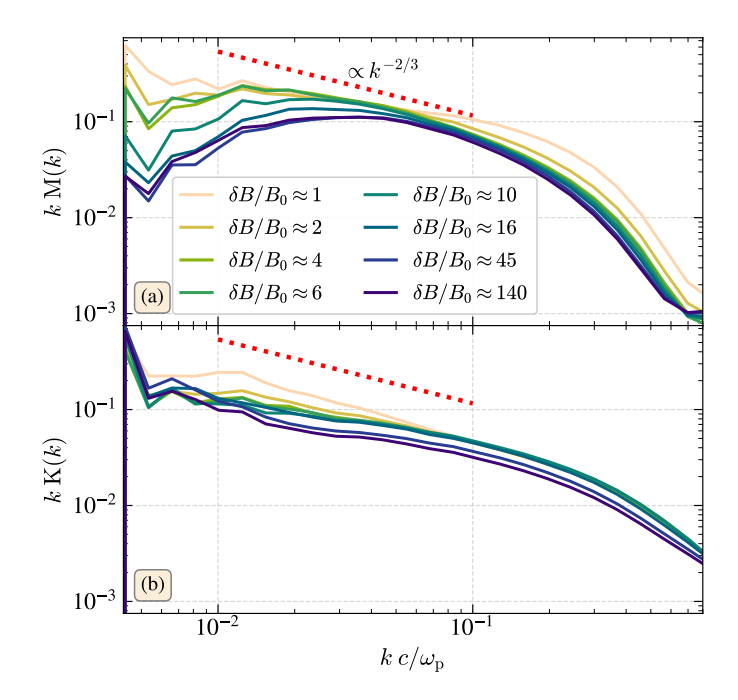


Figure 2. Isotropic magnetic (top panel) and kinetic (bottom panel) power spectra for each of our simulations with $L/(c/\omega_{\rm p})=2000$. The normalization of each spectrum is multiplied by the radial wavenumber, k, to show the energy in log-spaced bins; the integral over the magnetic spectrum yields $1/\beta$ (Equation (9)) and the integral over the kinetic spectrum yields the square of the sonic Mach number (Equation (6)). The red dotted lines in each panel indicate the Kolmogorov scaling $M(k) \propto K(k) \propto k^{-5/3}$ (A. Kolmogorov 1941). The magnetic power spectrum becomes noise-dominated at wavenumbers $k \, c/\omega_{\rm p} \gtrsim 0.7$, or physical scales below $\sim 9 \, c/\omega_{\rm p}$.

The multi-scale nature of the steady-state turbulent magnetic field, quantified in the spectra of Figure 2, can be seen qualitatively in Figure 3, which shows 2D slices (in the xy-plane) of $B/B_{\rm rms}$ – the local magnetic field strength normalized by the global rms magnetic field strength, $B_{\rm rms} \equiv \sqrt{\langle B^2 \rangle}$ – in our $\delta B/B_0 \approx 1$ (upper left), 4 (upper right), 10 (lower left), and 140 (bottom right) simulation boxes at late times. For $\delta B/B_0 \approx 140$, the flow has arranged the magnetic field into a folded sheet structure reminiscent of the saturated MHD dynamo (A. A. Schekochihin et al. 2004); as $\delta B/B_0$ decreases, the length of these structures decreases, yielding a more well-mixed turbulence. These turbulent

magnetic fields also possess abundant substructure at smaller scales. For example, the folding of field-lines has created an entire distribution of bent magnetic structures, with the smallest radii of curvature comparable to the magnetic dissipative scale. Additionally, current sheets (across which the magnetic field reverses rapidly) and reconnection plasmoids are especially prominent at larger $\delta B/B_0$.

The coherent structures at small scales in Figure 3 hint at the presence of intermittency in the turbulent magnetic field, or deviation of B from a Gaussian distribution. We quantify this in Figure 4, which shows renormalized probability density functions (PDFs) of increments of the x-component of the magnetic field 4 ,

$$\Delta B_x(r) \equiv |B_x(\mathbf{x} + \mathbf{r}) - B_x(\mathbf{x})|, \qquad (11)$$

for $\delta B/B_0 \approx 1$ (upper left), 4 (upper right), 10 (lower left), and 140 (lower right); for each $\delta B/B_0$, we sample increments at separations of $r/(c/\omega_{\rm p}) = 15, 45, 129,$ 357, and 999 (with lighter shades for larger r) to probe structure at a wide range of scales. We also subtract off the mean of each of our PDFs, $\overline{\Delta B_x}$, and divide by the standard deviation, $\Sigma_{\Delta B_r}$, so that our final distributions have a mean of zero and standard deviation of unity. As expected for an intermittent field, our renormalized PDFs increasingly deviate from Gaussian as we go to smaller scales (i.e., smaller separations, r) (Z.-S. She & E. Leveque 1994); at large scales the field is still sensitive to the driver (a Gaussian process), but nonuniformity in the turbulent cascade intensifies towards smaller scales, producing progressively more intense localized structures. The widespread presence of non-Gaussianity in our simulations motivates our study of intermittency in collisionless large-amplitude turbulence.

4. STATISTICS OF MAGNETIC FIELD-LINE BENDS AND REVERSALS

In the previous section, we showed that the magnetic field in collisionless large-amplitude turbulence is generically intermittent. Here, we focus on a specific class of intermittent structures present in the magnetic field: sharp magnetic field-line bends and rapid field reversals. These structures are formed by the stretching and folding of field lines into elongated geometries, across which the sign of the magnetic field varies over short length scales; at the ends of these structures, the magnetic field lines are tightly curved. These structures have direct

implications for particle transport and particle acceleration, which we explore in more depth in Section 6.

We can characterize field-line bends and reversals with two quantities: the magnitude of the field-line curvature, K_{\parallel} , and the inverse reversal scale, K_{\perp} (P. Kempski et al. 2023). Typically, the field-line curvature is defined as $|\hat{\mathbf{b}} \cdot \nabla \hat{\mathbf{b}}|$, where $\hat{\mathbf{b}} \equiv \mathbf{B}/B$ is the magnetic field unit vector; this can be understood as the variation of the magnetic field direction along the magnetic field itself. However, in this paper, we compute a slightly different quantity, removing any numerically introduced components of curvature along the field (P. Kempski et al. 2023):

$$K_{\parallel} \equiv \left| \hat{\mathbf{b}} \times \left(\hat{\mathbf{b}} \cdot \nabla \hat{\mathbf{b}} \right) \right|.$$
 (12)

We do not find significant discrepancy in our results when using K_{\parallel} vs. the traditional definition of curvature, but we do find that K_{\parallel} is more robust to numerical artifacts like grid downsampling.

To complement K_{\parallel} , which quantifies variation along the field, we define K_{\perp} to quantify variation across (or perpendicular to) the field. A common metric used to quantify variation across the field in the dynamo literature (e.g., A. A. Schekochihin et al. (2004); A. K. Galishnikova et al. (2022)) is

$$k_{\mathbf{J} \times \mathbf{B}} \equiv \frac{|\mathbf{J} \times \mathbf{B}|}{B^2} = \frac{|(\nabla \times \mathbf{B}) \times \mathbf{B}|}{B^2}.$$
 (13)

However, we follow P. Kempski et al. (2023) by defining

$$K_{\perp} \equiv k_{\mathbf{J} \times \mathbf{B}} - K_{\parallel} = \left| \hat{\mathbf{b}} \times \left(\hat{\mathbf{b}} \times \nabla \ln B \right) \right|.$$
 (14)

At a field-line bend, $K_{\parallel} \sim K_{\perp}$.

To begin our analysis of field-line curvature in collisionless large-amplitude turbulence, we show 2D PDFs of local magnetic field strength $(B/B_{\rm rms})$ vs. K_{\parallel} for each of our simulations with $L/(c/\omega_{\rm p}) = 2000$ in Figure 5. The (anti)correlation between field strength and curvature has been well-studied in MHD turbulence (e.g., A. Schekochihin et al. (2001); Y. Yang et al. (2019)); these studies find that $B \propto K_{\parallel}^{-1/2}$ at high K_{\parallel} , which corresponds to magnetic fields organized into structures that keep the magnetic tension force constant; we show this scaling with a red dotted line in Figure 5. However, in our PIC simulations, we find instead that $B \propto K_{\parallel}^{-3/4}$ (blue dotted line) is a consistently better fit across each of our $\delta B/B_0$. The high- K_{\parallel} tail steepens in the $\delta B/B_0 \approx 1$ and 2 cases, showing significant deviation from both $\propto B^{-1/2}$ and $\propto B^{-3/4}$; this is better visualized in the projected curves of $\langle B(K_{\parallel}) \rangle / B_{\rm rms}$ vs. K_{\parallel} shown in Figure 6. As we discuss in Section 5.2, the discrepancy between our measured B- K_{\parallel} correlation and

⁴ Our decision to take increments of B_x is arbitrary – we reach the same conclusions by taking increments of B_y or B_z .

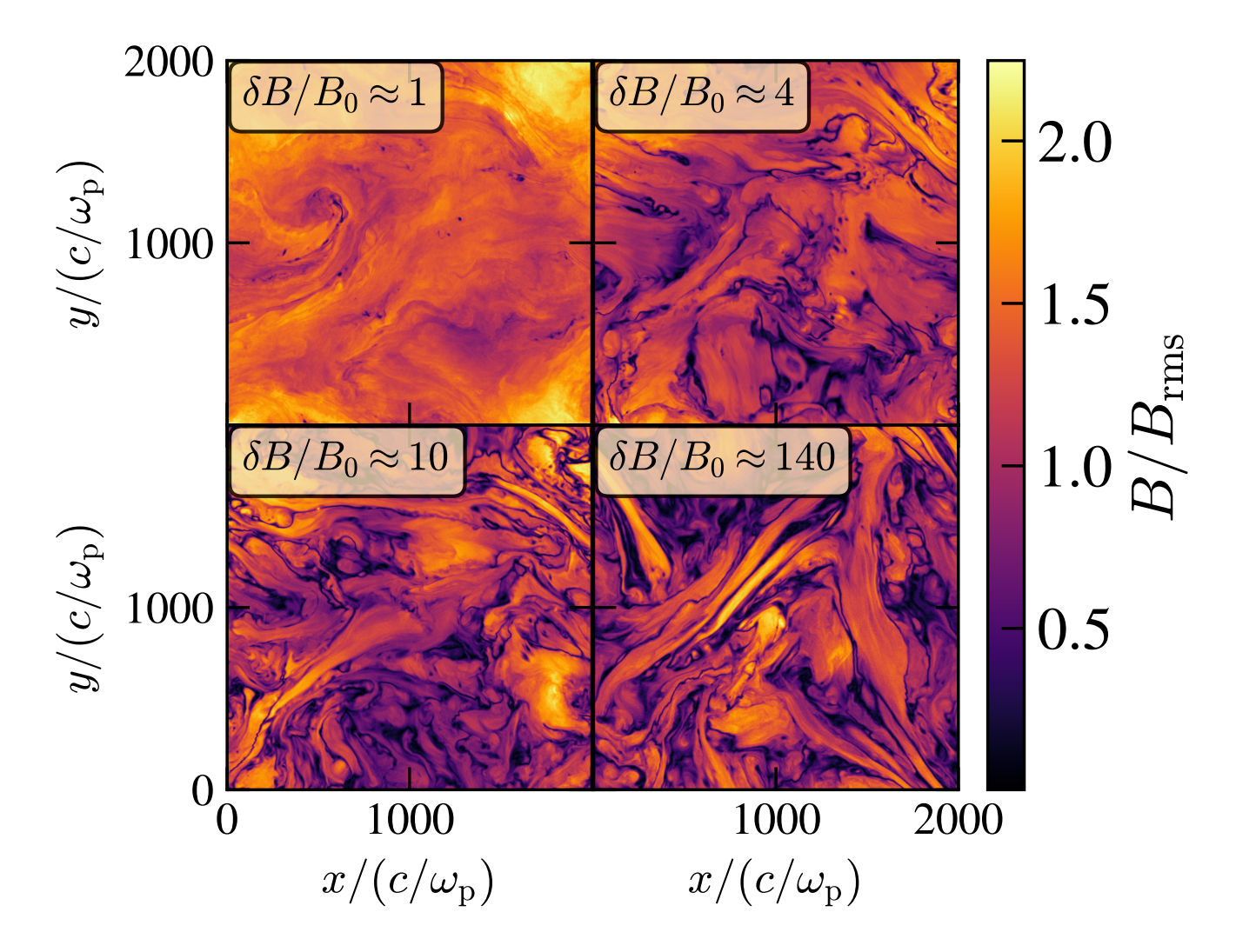


Figure 3. 2D slices (in the xy-plane) of $B/B_{\rm rms}$ – the local magnetic field strength normalized by the global rms magnetic field strength – at late times for our simulations with $\delta B/B_0 \approx 1$ (upper left), 4 (upper right), 10 (lower left), and 140 (lower right) and $L/(c/\omega_{\rm p}) = 2000$; brighter colors represent regions of stronger field.

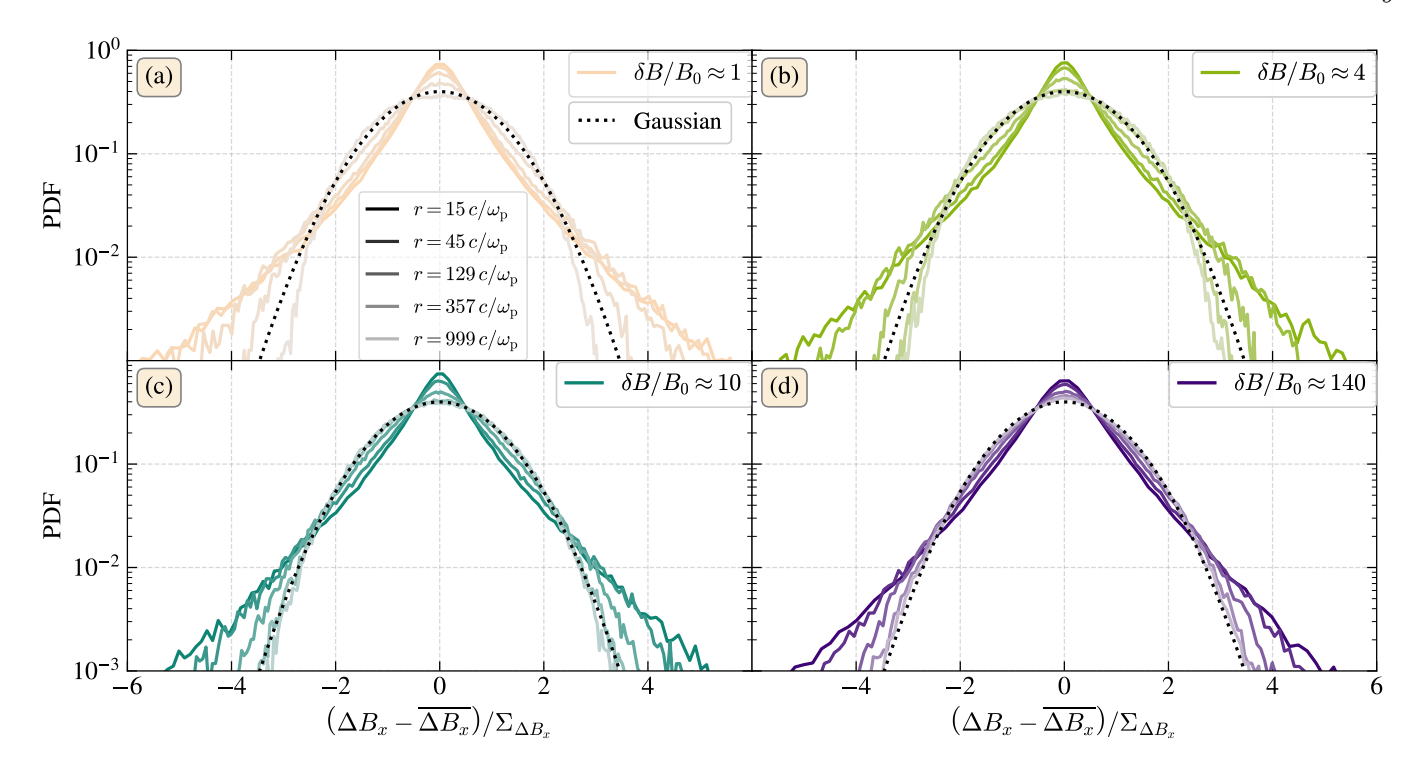


Figure 4. Renormalized probability density functions (PDFs) of increments of the x-component of the magnetic field (Equation (11)) for our simulations with $\delta B/B_0=1$ (upper left), 4 (upper right), 10 (lower left), and 140 (lower right) and $L/(c/\omega_{\rm P})=2000$. By subtracting the mean of the raw PDF, $\overline{\Delta B_x}$, and dividing by the standard deviation of the raw PDF, $\Sigma_{\Delta B_x}$, these renormalized PDFs have a mean of zero and a standard deviation of unity; the equivalent Gaussian distribution is shown as a dotted curve in each panel. For each $\delta B/B_0$, we show the renormalized PDF of field increments at five different separations, $r/(c/\omega_{\rm P})=15$, 45, 129, 357, and 999, with lighter shades for larger separations.

the MHD expectation across all $\delta B/B_0$ is likely due to the development of pressure anisotropy with respect to the magnetic field.

We can use our measurement of the $B\text{-}K_{\parallel}$ correlation to derive an expected scaling for the distribution function of field-line curvature, $P(K_{\parallel})$, at high K_{\parallel} . We find that, at large $\delta B/B_0$, the 1D PDF of magnetic field strength exhibits a $P(B) \propto B^{1/5}$ scaling in the range $10^{-1} \lesssim B/B_{\rm rms} \lesssim 1$ (see Figure 7), where the $B \propto K_{\parallel}^{-3/4}$ correlation holds. We therefore have

$$P(K_{\parallel}) dK_{\parallel} \propto P(B) dB$$

$$\implies P(K_{\parallel}) \propto K_{\parallel}^{-19/10}.$$
(15)

This scaling is close to the theoretically-derived $\propto K_{\parallel}^{-13/7}$ scaling expected in an MHD dynamo driven by a single-scale flow (A. A. Schekochihin et al. 2004); however, this agreement may be a coincidence given that our simulations develop full turbulent cascades. The slope of P(B) hardens slightly with decreasing $\delta B/B_0$, reaching $P(B) \propto B$ by $\delta B/B_0 \approx 4$; therefore, we expect a scaling closer to $P(K_{\parallel}) \propto K_{\parallel}^{-2.5}$ for smaller $\delta B/B_0$. This $\propto K_{\parallel}^{-2.5}$ scaling has been observed both in MHD simu-

lations (Y. Yang et al. 2019) and in the solar wind (R. Bandyopadhyay et al. 2020; S. Y. Huang et al. 2020).

In Figure 8, we plot 1D PDFs of K_\parallel and K_\perp for each of our simulations with $L/(c/\omega_{\rm p}) = 2000$. For visualization purposes, we split the PDFs into two groups: the dynamo-like cases with $\delta B/B_0 \gtrsim 10$ (bottom panel) and the Kolmogorov-like cases (i.e., the cases affected by a dynamically important mean field, where the magnetic spectrum develops a Kolmogorov-like scaling) with $\delta B/B_0 \lesssim 6$ (top panel). Each of the PDFs of K_{\parallel} displays a prominent power-law tail extending towards high K_{\parallel} , clearly illustrating the intermittency (i.e., non-Gaussianity) of sharp field-line bends; we show the ${\rm P}(K_{\parallel}) \propto K_{\parallel}^{-2}$ (or $K_{\parallel} \, {\rm P}(K_{\parallel}) \propto K_{\parallel}^{-1})$ power-law scaling with a red dotted line and the P(K_{\parallel}) $\propto K_{\parallel}^{-2.5}$ (or $K_{\parallel} P(K_{\parallel}) \propto K_{\parallel}^{-1.5}$) scaling with a blue dotted line. As expected, $\mathrm{P}(K_{\parallel}) \propto K_{\parallel}^{-2}$ is an excellent fit to our larger $\delta B/B_0$ cases (especially $\delta B/B_0 \approx 140$), while $P(K_{\parallel}) \propto K_{\parallel}^{-2.5}$ is an excellent fit to our smaller $\delta B/B_0$ cases (especially $\delta B/B_0 \approx 6$). The K_{\parallel} PDFs for $\delta B/B_0 \approx 1$ and 2 exhibit much steeper slopes than $P(K_{\parallel}) \propto K_{\parallel}^{-2.5}$; these cases also stand out in our plots of $\langle B \rangle$ vs. K_{\parallel} (Figure 6) and of P(B) (Figure 7), indi-

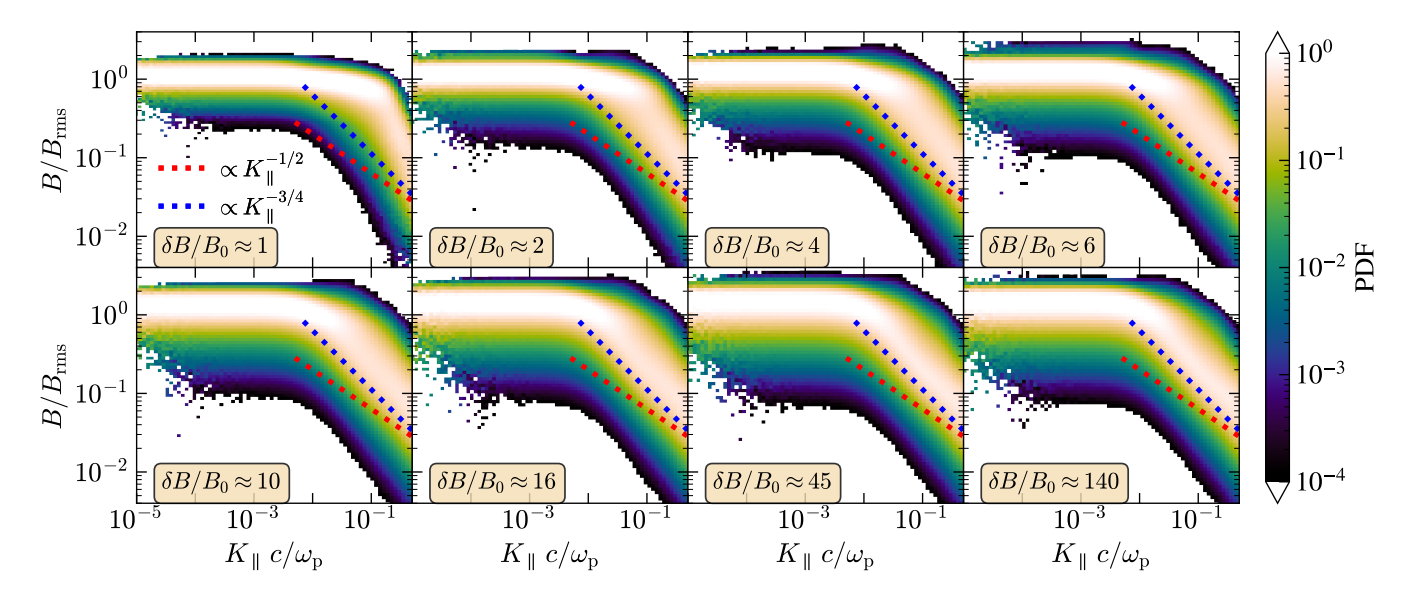


Figure 5. 2D PDFs of the local magnetic field strength, $B/B_{\rm rms}$, vs. the local field-line curvature, K_{\parallel} , for each of our simulations with $L/(c/\omega_{\rm P})=2000$ (see panel labels). The red dotted line in each panel shows the scaling $B \propto K_{\parallel}^{-1/2}$ (expected in MHD, e.g., A. A. Schekochihin et al. (2004)), while the blue dotted line shows $B \propto K_{\parallel}^{-3/4}$. To increase the contrast in the high- K_{\parallel} tails of these PDFs, we normalize the PDFs such that the integral over the 1D PDF of $B/B_{\rm rms}$ at each K_{\parallel} is unity.

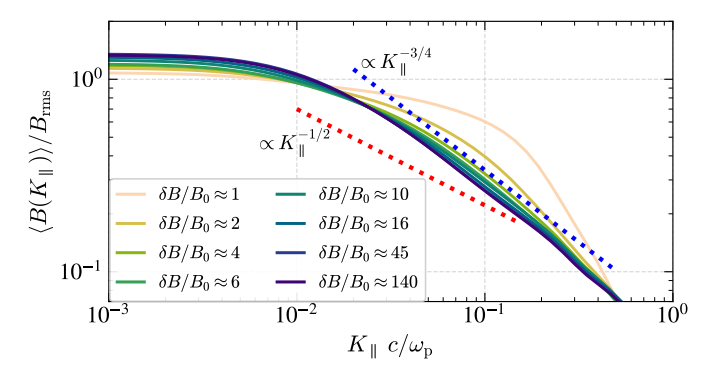


Figure 6. Average magnetic field strength, $\left\langle B(K_{\parallel})\right\rangle/B_{\rm rms}$, as a function of field-line curvature, K_{\parallel} , for each of our simulations with $L/(c/\omega_{\rm p})=2000$. The red dotted line shows the scaling $B \propto K_{\parallel}^{-1/2}$, while the blue dotted line shows $B \propto K_{\parallel}^{-3/4}$.

cating that they are governed by different physics than the larger $\delta B/B_0$ cases.

In light of the above measurements, we caution that the power-law slope of the K_{\parallel} PDF depends on $L/(c/\omega_{\rm p})$; in Figure 17, we show that, for smaller $\delta B/B_0$, the power-law slopes for $L/(c/\omega_{\rm p})=1000$ and $L/(c/\omega_{\rm p})=2000$ match nicely $(\delta B/B_0\approx 1$ shows exceptional agreement between the power-law slopes across all three box sizes), while we require simulations at larger $L/(c/\omega_{\rm p})$ to confirm that our higher- $\delta B/B_0$ cases are converged.

The PDFs of K_{\perp} strongly deviate from their MHD counterparts: the K_{\perp} PDFs in MHD have rounded

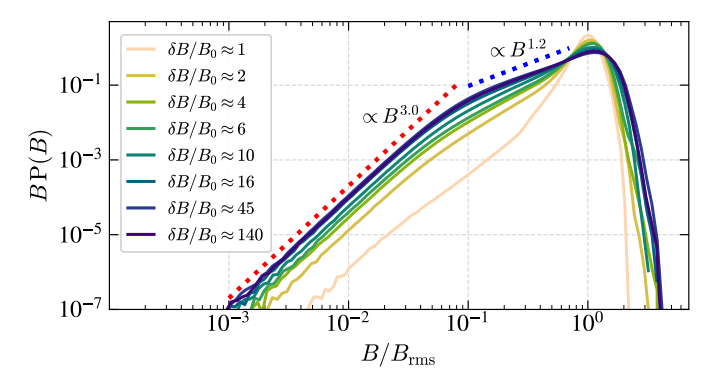


Figure 7. 1D PDFs of $B/B_{\rm rms}$, the local magnetic field strength normalized to the global rms magnetic field strength, for each of our simulations with $L/(c/\omega_{\rm P})=2000$. The red dotted line indicates a scaling of $P(B) \propto B^{2.0}$ (or $BP(B) \propto B^{3.0}$) and the blue dotted line indicates $P(B) \propto B^{0.2}$ (or $BP(B) \propto B^{1.2}$).

peaks that drop off smoothly towards the resistive scale (P. Kempski et al. 2023), while our K_{\perp} PDFs show shallow power-law slopes for $\delta B/B_0 \lesssim 10$ and remarkably flat, extended plateaus for $\delta B/B_0 \gtrsim 16$. These plateaus could be due to reconnection plasmoids with a broad size distribution; future work should determine the precise contribution of reconnection physics to the K_{\parallel} and K_{\perp} PDFs. For each of the dynamo-like cases, the peak of the K_{\perp} PDF lies at much smaller scales than that of the K_{\parallel} PDF, consistent with the MHD dynamo picture of elongated magnetic folds with large coherence lengths along the local magnetic field and small coher

ence lengths across the field (A. A. Schekochihin et al. 2004; F. Rincon 2019; A. K. Galishnikova et al. 2022); this contrasts with the small $\delta B/B_0$ cases, for which the peaks of the K_{\parallel} and K_{\perp} PDFs are nearly overlapping, suggesting that, for most bends, the coherence lengths along and across the field are similar.

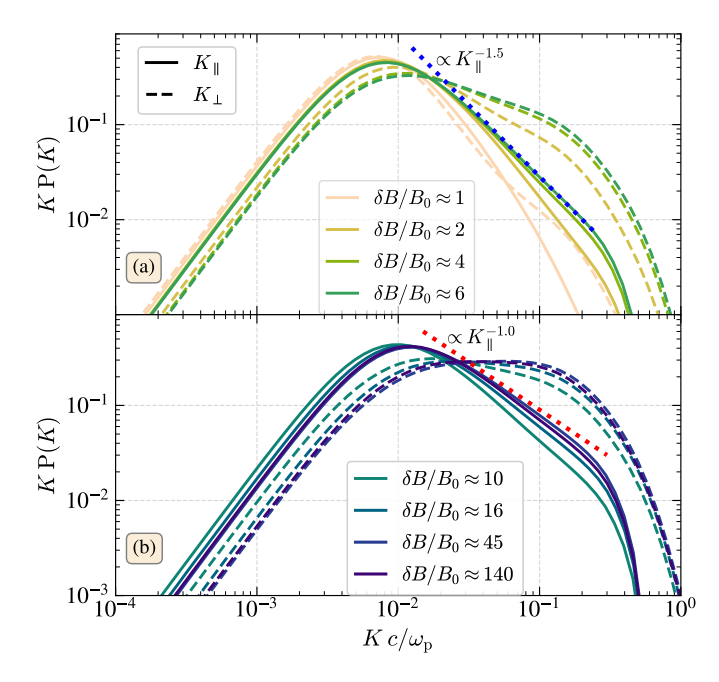


Figure 8. 1D PDFs of K_{\parallel} (solid curves; Equation (12)) and K_{\perp} (dashed curves; Equation (14)) for each of our simulations with $L/(c/\omega_{\rm p})=2000$, split between the dynamolike cases with $\delta B/B_0\gtrsim 10$ (bottom panel) and the Kolmogorov-like cases with $\delta B/B_0\lesssim 6$ (top panel). The red dotted line in the bottom panel indicates a power-law scaling $K_{\parallel}\,\mathrm{P}(K_{\parallel})\propto K_{\parallel}^{-1}$ (or $\mathrm{P}(K_{\parallel})\propto K_{\parallel}^{-2}$, as derived in Equation (15)) and the blue dotted line in the top panel indicates a scaling $K_{\parallel}\,\mathrm{P}(K_{\parallel})\propto K_{\parallel}^{-1.5}$ (or $\mathrm{P}(K_{\parallel})\propto K_{\parallel}^{-2.5}$, as seen in MHD, e.g., Y. Yang et al. (2019), and the solar wind, e.g., R. Bandyopadhyay et al. (2020)).

We can directly connect our statistics of K_{\parallel} to particle transport through collisionless large-amplitude turbulence. While we reserve a more comprehensive discussion of particle transport for Section 6.1, here we analyze statistics pertinent to a mode of particle scattering referred to as "resonant curvature scattering" (P. Kempski et al. 2023; M. Lemoine 2023; J. Lübke et al. 2025): if a charged particle's gyroradius at a field-line bend is comparable to or slightly larger than the bend's radius of curvature, then the particle will see a full field reversal during a gyro-orbit, thus violating conservation of magnetic moment and yielding an order-unity change in the particle's pitch angle. Quantitatively, we write the condition for resonant curvature scattering as $K_{\parallel} r_{\rm g} \gtrsim 1$,

where

$$r_{\rm g} \equiv \frac{\gamma mc^2}{aB} \tag{16}$$

is the particle's instantaneous gyroradius in a magnetic field of strength B; γ is the particle's Lorentz factor, m is its mass, and q is its charge. Since $r_{\rm g}$ at fixed γ carries spatial-dependence through the local magnetic field strength, it is convenient to absorb this spatial dependence into the curvature statistics by defining the mean gyroradius,

$$\overline{r_{\rm g}} \equiv r_{\rm g} \frac{B}{B_{\rm rms}},$$
 (17)

and the renormalized curvature (M. Lemoine 2023),

$$\hat{K}_{\parallel} \equiv K_{\parallel} \frac{B_{\rm rms}}{R},\tag{18}$$

such that the condition for resonant curvature scattering becomes

$$K_{\parallel} r_{\rm g} = \hat{K}_{\parallel} \overline{r_{\rm g}} \gtrsim 1.$$
 (19)

To build PDFs that more accurately represent the probability of resonant curvature scattering, we further filter out curvature that does not contribute to scattering (e.g., field-line bends on scales much below the mean gyroradius or field-line kinks where high curvature only appears transiently). More precisely, we "coarse grain" the magnetic field below a scale ℓ (representing $\overline{r_{\rm g}}$) by applying a uniform averaging filter of side-length ℓ to each cell in our box; we write the resulting smoothed and renormalized curvature as $\hat{K}_{\parallel,\ell}$. In this way, integrating the 1D PDF of $\hat{K}_{\parallel,\ell}\ell$ for $\hat{K}_{\parallel,\ell}\ell \gtrsim 1$ yields a rough volume-filling fraction of viable scatterers for a particle with $\overline{r_{\rm g}} \sim \ell$; we convert these volume-filling fractions to mean free paths in Section 6.1.

In Figure 9, we show 1D PDFs of $\hat{K}_{\parallel,\,\ell}\ell$ for our $\delta B/B_0 \approx 1$ (upper left), 4 (upper right), 10 (bottom left), and 140 (bottom right) simulations with $L/(c/\omega_{\rm p}) = 2000$; for each $\delta B/B_0$, we show the PDFs for five different smoothing scales, $\ell/(c/\omega_{\rm p}) = 15$, 45, 129, 357, and 999. As we smooth at larger scales and remove more small-scale bends, the exponential cutoffs of the power-law tails of the PDFs gradually disappear; this smoothing produces nearly Gaussian PDFs at large ℓ for the small $\delta B/B_0$ cases (i.e., $\delta B/B_0 \approx 1$ and 4), yet it still leaves extended power-laws at larger $\delta B/B_0$ (i.e., $\delta B/B_0 \approx 10$ and 140). Additionally, the peak of these PDFs systematically shifts to lower $\hat{K}_{\parallel,\,\ell}\ell$ as we increase ℓ , as seen in MHD (M. Lemoine 2023).

In this section, we have found that certain properties of the intermittent magnetic field in collisionless large-amplitude turbulence – such as the shape of the 1D PDF of field-line curvature, the $K_{\parallel}^{-2.5}$ scaling of this PDF at high K_{\parallel} for moderate $\delta B/B_0$, and the response of this

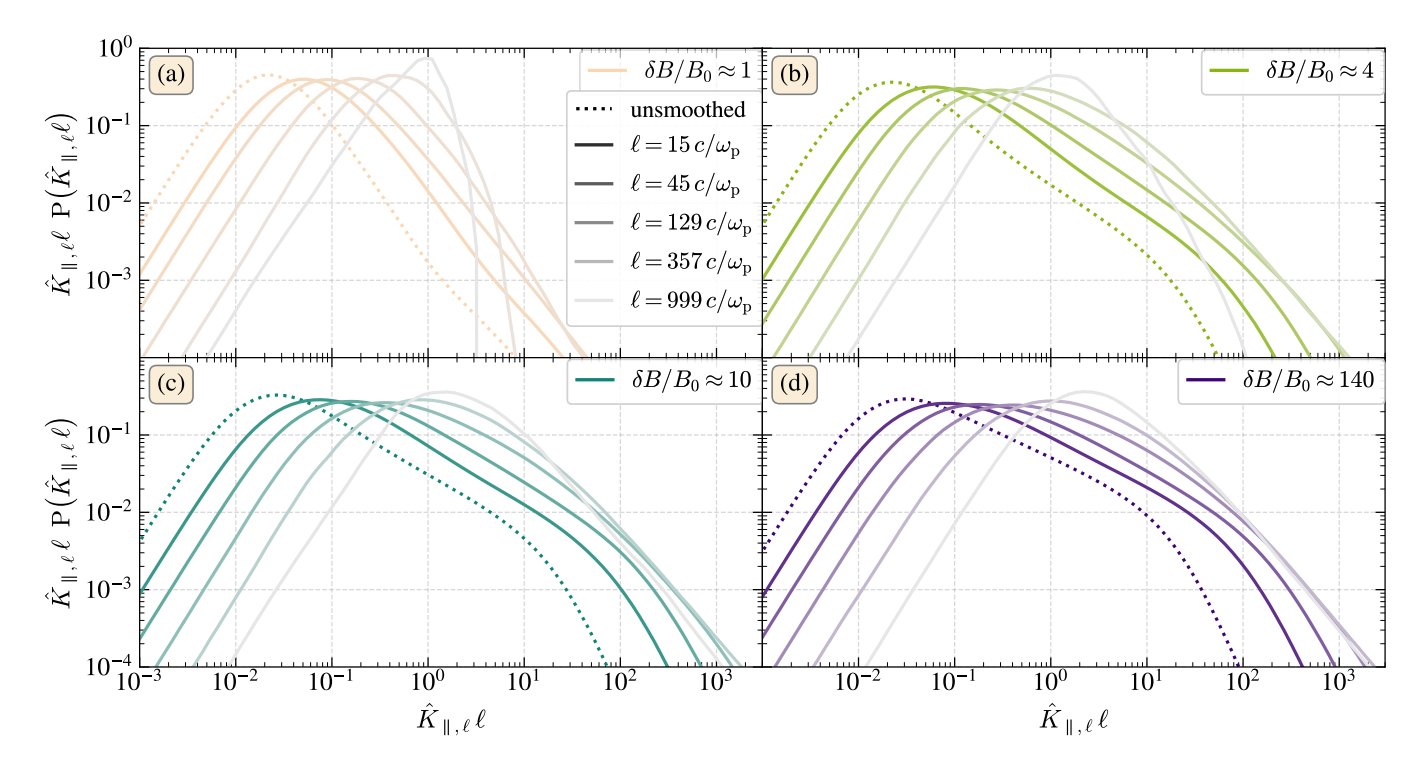


Figure 9. PDFs of the smoothed renormalized curvature, $\hat{K}_{\parallel,\ell}$ (Equation (18)), multiplied by the smoothing scale, ℓ , for our simulations with $\delta B/B_0 \approx 1$ (upper left), 4 (upper right), 10 (lower left), and 140 (lower right) and $L/(c/\omega_p) = 2000$. For each $\delta B/B_0$, we show the PDFs of $\hat{K}_{\parallel,\ell}$ for five different smoothing scales, $\ell/(c/\omega_p) = 15$, 45, 129, 357, and 999, with lighter shades for larger ℓ ; the PDFs of renormalized curvature with no smoothing are depicted with dotted curves.

PDF to coarse-graining – broadly resemble their equivalent MHD measurements. However, these measurements generally disagree in detail, with small discrepancies in the correlation between B and K_{\parallel} and, consequently, in the power-law slopes of the PDFs of K_{\parallel} for large $\delta B/B_0$. In the next section, we explore what might be causing this disagreement.

5. THE IMPACT OF PRESSURE ANISOTROPY ON COLLISIONLESS LARGE-AMPLITUDE TURBULENCE

A major difference between collisionless turbulence and its MHD counterpart is the ability of the former to generate pressure anisotropy. At $\beta \gtrsim 1$ – which is the case for all of our simulations – pressure anisotropy triggers kinetic instabilities (S. P. Gary 1993) that can modify the properties of the turbulence. In Section 5.1, we provide evidence of these instabilities in our simulated turbulence; in Section 5.2, we show that, although these instabilities themselves do not significantly affect the statistics of K_{\parallel} and K_{\perp} , the underlying pressure anisotropy may explain the discrepancy with MHD detailed in Section 4.

5.1. Evidence of pressure-anisotropy-induced instabilities

In a collisionless magnetized plasma, changes in the magnetic field strength affect perpendicular and parallel particle motions in different ways due to the conservation of adiabatic invariants; macroscopically, this is quantified by the CGL equations (G. F. Chew et al. 1956),

$$\frac{P_{\perp}}{nB} = \text{const.} \tag{20}$$

and

$$\frac{P_{\parallel}B^2}{n^3} = \text{const.},\tag{21}$$

where P_{\perp} is the pressure perpendicular to the magnetic field, P_{\parallel} is the pressure parallel to the field, and n is the number density (for a single species). These equations tell us that, at fixed density, an increase in magnetic field strength causes an increase in P_{\perp} but a decrease in P_{\parallel} , generating pressure anisotropy. In the limit of incompressible turbulence, the magnetic field is strengthened when field lines are stretched and weakened when field lines are bent, so we expect positive pressure anisotropy (i.e., $P_{\perp}/P_{\parallel} > 1$) in the former case and negative anisotropy (i.e., $P_{\perp}/P_{\parallel} > 1$) in the latter.

Since our turbulence has $\beta \gtrsim 1$, we expect pressure anisotropy to trigger the mirror and firehose instabili-

ties, which themselves regulate the anisotropy (F. Rincon et al. 2015; C.-S. Jao & L.-N. Hau 2020; L. Arzamasskiy et al. 2023); mirror modes grow in regions of positive pressure anisotropy when

$$P_{\perp}/P_{\parallel} > 1 + 1/\beta_{\parallel}$$
 (22)

and (parallel) firehose modes grow in regions of negative pressure anisotropy when

$$P_{\perp}/P_{\parallel} \lesssim 1 - 2/\beta_{\parallel},\tag{23}$$

where $\beta_{\parallel} \equiv P_{\parallel}/(B^2/8\pi)$ is the ratio of parallel pressure to magnetic pressure. Mirror and firehose fluctuations grow fastest at scales comparable to the anisotropic species' thermal Larmor radius (in our case, the thermal electron or positron Larmor radius) and grow rapidly compared to the rate of macroscopic deformation; this allows the fluctuations to almost immediately feed back onto the flow (J. Squire et al. 2019, 2023; S. Majeski et al. 2024).

One way in which mirror and firehose instabilities affect the plasma is by imposing a delimiting effect on the accessible phase space of the turbulence, pinning the system around their instability thresholds (S. D. Bale et al. 2009; F. Rincon 2019). We illustrate this effect in Figure 10 by showing "Brazil plots," or 2D PDFs of P_{\perp}/P_{\parallel} vs. β_{\parallel} , for each of our simulations with $L/(c/\omega_{\rm p})=2000$; we indicate the mirror threshold with a solid red curve and the firehose threshold with a dashed red curve. For each $\delta B/B_0$, the vast majority of the probability density lies just within the stable region and a smaller but significant amount of the PDF straddles the instability thresholds. As $\delta B/B_0$ decreases, the central contour shifts and distorts so that progressively less of the PDF lies outside the stable regions; by $\delta B/B_0 \approx 1$ (our lowest- β case), we seem to enter a different regime where the central contour shows minimal correlation with the instability thresholds.

While Figure 12 provides a qualitative picture of the volume-filling fractions of mirror- and firehose-unstable regions in our simulated turbulence, we quantify this in Figure 11 as a function of both $\delta B/B_0$ and $L/(c/\omega_p)$. For all $\delta B/B_0$ except $\delta B/B_0 \approx 1$, the mirror-unstable fraction is larger than the firehose-unstable fraction by a factor of a few; in the large- $\delta B/B_0$ dynamo-like cases with $L/(c/\omega_p) = 2000$, $\sim 20\%$ of the volume is mirror-unstable and $\sim 5\%$ of the volume is firehose-unstable, with both of these fractions declining steadily for $\delta B/B_0 \lesssim 16$, giving $\sim 4\%$ mirror-unstable and $\sim 2\%$ firehose-unstable for $\delta B/B_0 \approx 2$ and $\sim 0.4\%$ mirror-unstable and $\sim 2\%$ firehose-unstable for $\delta B/B_0 \approx 1$. Consistently, the unstable fraction decreases as $L/(c/\omega_p)$ increases; this could be because weaker driving

(i.e., a smaller rate of strain, $u_{\rm rms}/L$) at larger $L/(c/\omega_{\rm p})$ is less effective at generating pressure anisotropy and can only push the plasma marginally past the instability thresholds. However, for $2 \lesssim \delta B/B_0 \lesssim 45$, there is evidence of asymptotic convergence with increasing $L/(c/\omega_{\rm p})$, since the difference in the unstable fraction is less pronounced between $L/(c/\omega_{\rm p})=1000$ and 2000 than it is between $L/(c/\omega_{\rm p})=500$ and 1000.

While mirror and firehose modes are responsible for regulating the pressure anisotropy, these are not the only possible Larmor-scale fluctuations triggered by the anisotropy. For example, cyclotron-type fluctuations like whistler waves – which, like mirror modes, grow in regions of positive pressure anistropy (L. Sironi & R. Narayan 2015) – are likely also present in our turbulence, but their impact is not obvious. Since these cyclotrontype fluctuations are usually expected for $\beta < 1$, they may be abundant in our turbulence with smaller $\delta B/B_0$, possibly explaining why the central contour of the Brazil plot for $\delta B/B_0 \approx 1$ (in Figure 10) is not well-defined by the mirror and firehose thresholds. However, a quantitative investigation of the role of cyclotron-type instabilities in collisionless large-amplitude turbulence is outside the scope of this work and should be performed in an electron-ion plasma where ion cyclotron fluctuations and whistler fluctuations will not be degenerate in scale.

5.2. Pressure anisotropy and field-line curvature

Growing mirror and firehose fluctuations each affect the morphology of the local magnetic field: where field lines are strengthened by the flow and become mirror unstable, perpendicular pressure forces cause field lines to bubble up, creating microscopic magnetic mirrors or bottles; where field lines are weakened by the flow and become firehose unstable, parallel pressure forces squeeze and pinch flux tubes, exacerbating tight fieldline bends. Therefore, we expect these fluctuations to modify the field-line curvature throughout our simulated turbulence.

We can gain some qualitative insight into the correlation between pressure anisotropy and field-line curvature by making Brazil plots colored by the average K_{\parallel} in each bin; this is shown in Figure 12 for each of our simulations with $L/(c/\omega_{\rm p})=2000$. Two patterns are recognizable across all $\delta B/B_0$: first, curvature increases towards higher β_{\parallel} (or, equivalently, towards lower magnetic field strength and weaker magnetic tension) where field lines are easier to bend; and second, curvature is enhanced in regions where the pressure anisotropy exceeds the mirror and firehose thresholds. These trends show little dependence on $\delta B/B_0$, even down to $\delta B/B_0 \approx 1$. In other words, in each of our simulations, regions with

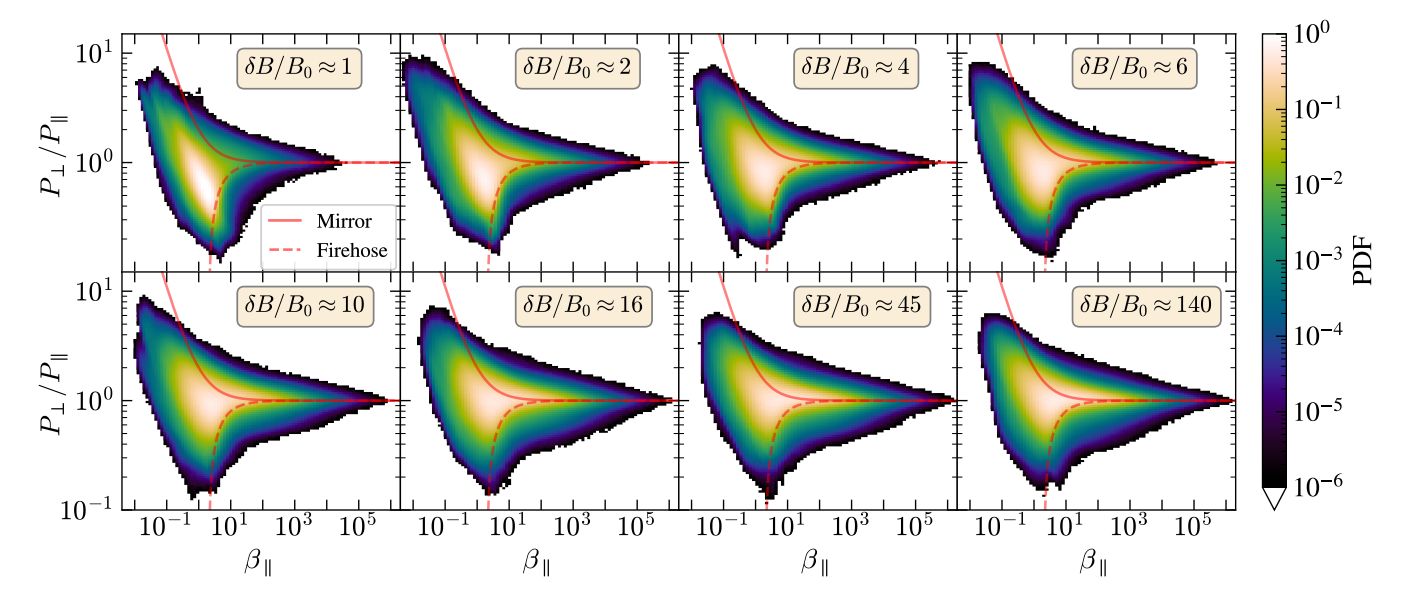


Figure 10. Brazil plots, or 2D PDFs of P_{\perp}/P_{\parallel} vs. β_{\parallel} , for each of our simulations with $L/(c/\omega_{\rm P})=2000$ (see panel labels). In each panel, the mirror instability threshold, $P_{\perp}/P_{\parallel}>1+1/\beta_{\parallel}$, is plotted as the solid red line and the firehose instability threshold, $P_{\perp}/P_{\parallel}<1-2/\beta_{\parallel}$, is plotted as the dashed red line.

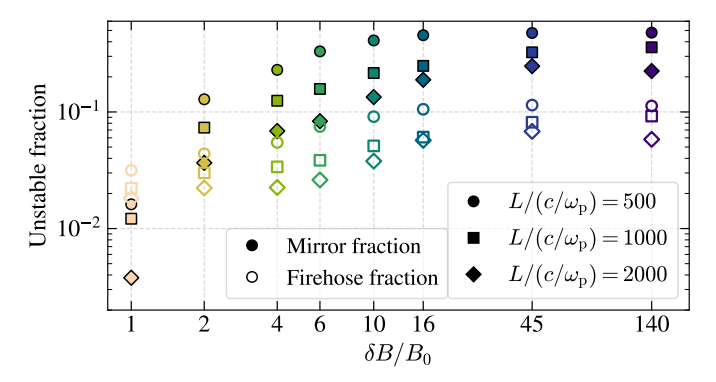


Figure 11. Volume-filling fractions of mirror-unstable (filled markers) and firehose-unstable (empty markers) regions in each of our simulations as a function of both $\delta B/B_0$ (shown on the horizontal axis) and $L/(c/\omega_{\rm p})$ (differentiated by marker style); simulations with $L/(c/\omega_{\rm p})=500$ are represented by circular markers, those with $L/(c/\omega_{\rm p})=1000$ by square markers, and those with $L/(c/\omega_{\rm p})=2000$ by diamond markers.

intense curvature are co-spatial with mirror and firehose fluctuations.

To gauge the impact of mirror and firehose fluctuations on the statistics of K_{\parallel} , we perform a simple experiment in which we compute the 1D PDF of K_{\parallel} using only cells that are mirror- and firehose-stable, but keep the overall sampling in β_{\parallel} the same as in the full data set; in practice, we assign each cell a weight equal to $P_{\rm total}(\beta_{\parallel})/P_{\rm stable}(\beta_{\parallel})$ for that cell's local value of β_{\parallel} , where $P_{\rm total}(\beta_{\parallel})$ is the 1D PDF of β_{\parallel} computed using the full domain and $P_{\rm stable}(\beta_{\parallel})$ is the PDF computed from only stable cells. We find that this reweighted PDF of

 K_{\parallel} in stable regions closely matches the global PDF of K_{\parallel} , indicating that mirror and firehose-unstable regions do not contribute substantially to the PDF of K_{\parallel} . This is likely due to the small volume-filling fractions of mirror and firehose fluctuations in our turbulence (Figure 11); we speculate that these fluctuations would play a more significant role at higher β , as seen in D. A. St-Onge & M. W. Kunz (2018).

However, while the mirror and firehose fluctuations themselves do not significantly impact the statistics of curvature, the underlying pressure anisotropy can still have an effect. In a collisionless magnetized plasma, pressure anisotropy with respect to the magnetic field contributes to an effective field-line tension of the form $B^2/4\pi + P_{\perp} - P_{\parallel}$, which can be derived by taking the first velocity moment of the Vlasov equation in the driftkinetics limit (R. M. Kulsrud et al. 1980). Since the $B \propto K_{\parallel}^{-1/2}$ scaling in MHD is derived by balancing the magnetic tension with the velocity field (A. Schekochihin et al. 2001), we expect that a similar scaling should hold in our collisionless turbulence if we incorporate the effective tension contributed by the pressure anisotropy. Therefore, instead of plotting 2D PDFs of B vs. K_{\parallel} as we did in Figure 5, in Figure 13 we plot 2D PDFs of the square root of the effective field-line tension, $\sqrt{|B^2/4\pi + P_{\perp} - P_{\parallel}|}$, vs. K_{\parallel} . Across all $\delta B/B_0$, the high- K_{\parallel} tail of the PDF is remarkably well-fit by the scaling $\sqrt{|B^2/4\pi + P_{\perp} - P_{\parallel}|} \propto K_{\parallel}^{-1/2}$, as expected. Evidently, pressure anisotropy accounts for at least some of the discrepancy in curvature statistics between colli-

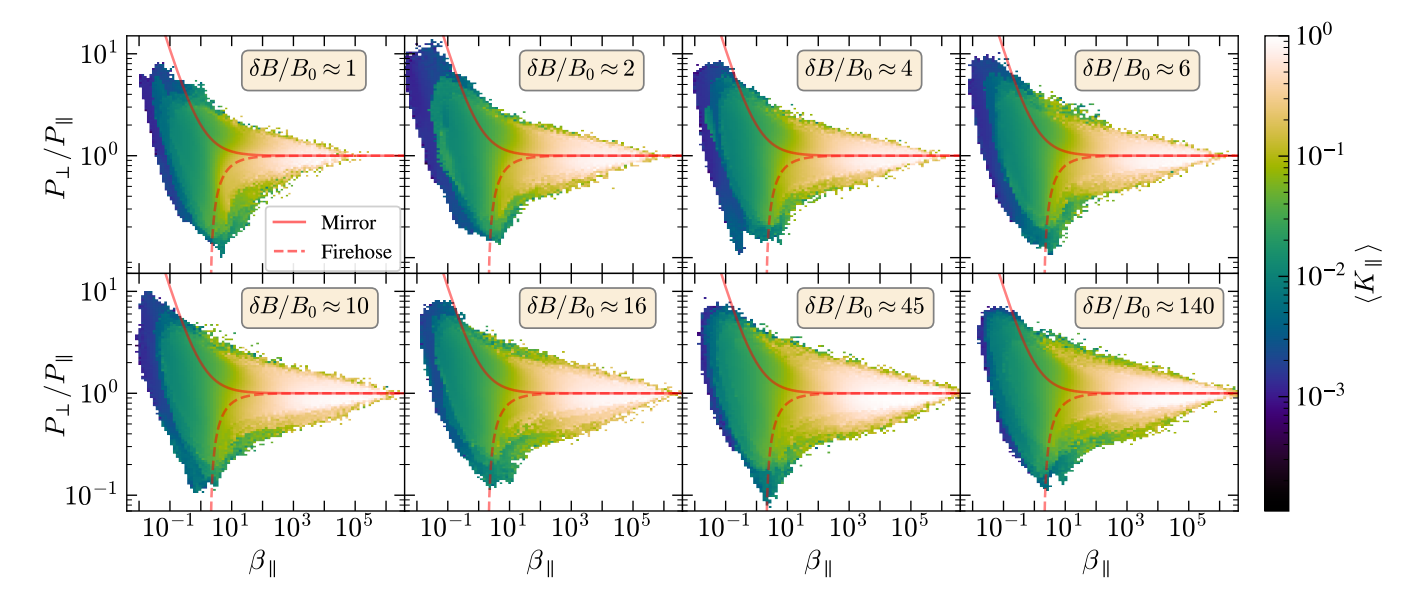


Figure 12. Brazil plots colored by local curvature, $\langle K_{\parallel} \rangle$, for each of our simulations with $L/(c/\omega_{\rm p}) = 2000$ (see panel labels). To maintain adequate dynamical contrast, the color range in each panel is normalized to the panel's maximum $\langle K_{\parallel} \rangle$. In each panel, the mirror instability threshold (Equation (22)) is plotted as the solid red line and the firehose instability threshold (Equation (23)) is plotted as the dashed red line.

sionless large-amplitude turbulence and its MHD counterpart.

6. DISCUSSION

6.1. Implications for particle transport in collisionless large-amplitude turbulence

Our results have immediate implications for particle transport through the turbulent collisionless plasma filling both the hot interstellar medium (ISM) of galaxies – where $\delta B/B_0$ can reach values of a few (M. Haverkorn 2015) – and the intracluster medium (ICM) of galaxy clusters – where $\delta B/B_0$ is likely large (A. Bonafede et al. 2010). While we do not track individual particles or field lines in this work (though we plan to in follow-up work), the statistics we have collected allow us to make a few quantitative estimates pertinent to particle transport. Specifically, we can estimate the mean free path to non-adiabatic "resonant" curvature scattering and we can measure the probability of scattering off of microscale mirror fluctuations.

As a particle approaches a field-line bend, its fate is determined by its instantaneous gyroradius, $r_{\rm g}$ (Equation (16)), and the curvature of the bend, K_{\parallel} : if $K_{\parallel}r_{g}\gg 1$ then the particle will detach from the field line and drift away at the bend; if $K_{\parallel}r_{g}\ll 1$ then the particle will stay attached to the field line and exactly follow the bend; and if $K_{\parallel}r_{g}\gtrsim 1$ then the particle will sample a full field reversal in a single gyro-orbit, subsequently suffering an order-unity change in its pitch angle. Field-line curvature can therefore confine par-

ticles in two ways: by adiabatically guiding particles through field-line bends (when $K_{\parallel}r_g \ll 1$) or by non-adiabatically (or "resonantly") scattering particles in pitch angle (when $K_{\parallel}r_g \gtrsim 1$).

As discussed towards the end of Section 4, we can estimate a particle's mean free path to resonant curvature scattering by integrating over 1D PDFs of the renormalized curvature (\hat{K}_{\parallel} , Equation (18)) coarse-grained on a scale ℓ ; these PDFs of $\hat{K}_{\parallel,\,\ell}\,\ell$ were shown in Figure 9. Taking $\hat{K}_{\parallel,\,\ell}\,\ell\gtrsim 1$ to be the condition for resonant curvature scattering of a particle with $\overline{r_{\rm g}}\sim\ell$ (for $\overline{r_{\rm g}}$ the particle's mean gyroradius, Equation (17)) – meaning that the integral of the PDF of $\hat{K}_{\parallel,\,\ell}\,\ell$ above unity gives the volume-filling fraction of regions where curvature scattering is possible – we can estimate the mean free path to resonant curvature scattering with (M. Lemoine 2023)

$$\lambda_{\text{mfp, curve}} = \frac{\ell}{\int_{1}^{\infty} P_{\hat{K}_{\parallel \ell} \ell}(x) \ dx}, \tag{24}$$

where $x \equiv \hat{K}_{\parallel,\,\ell}\,\ell$ and $P_{\hat{K}_{\parallel,\,\ell}\,\ell}(x)$ is the PDF of x. In Figure 14, we show the mean free paths computed for $\ell/(c/\omega_{\rm p}) \sim \overline{r_{\rm g}}/(c/\omega_{\rm p}) = 15,\,45,\,129,\,357,\,$ and 999 for each of our simulations with $L/(c/\omega_{\rm p}) = 2000.$ We find two salient trends in $\lambda_{\rm mfp,\,curve}$. First, $\lambda_{\rm mfp,\,curve}$ increases with decreasing $\delta B/B_0$; this is consistent with the gradual reduction in probability density at high K_{\parallel} as $\delta B/B_0$ decreases in Figure 8. Second, $\lambda_{\rm mfp,\,curve}$ increases with increasing $\overline{r_{\rm g}}$, since coarse-graining at larger $\ell \sim \overline{r_{\rm g}}$ removes more small-scale bends; this trend confirms the picture that particles with larger $\overline{r_{\rm g}}$ can res-

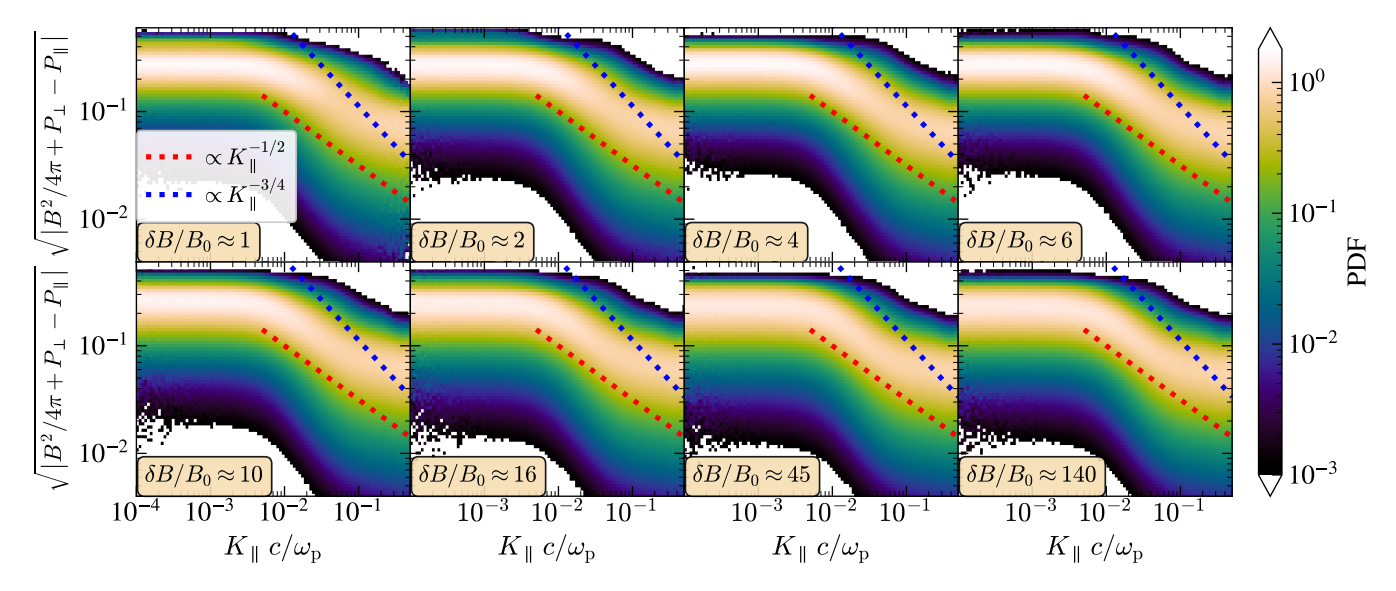


Figure 13. 2D PDFs of the square root of the effective magnetic tension, $\sqrt{|B^2/4\pi + P_{\perp} - P_{\parallel}|}$, vs. the local field-line curvature, K_{\parallel} , for each of our simulations with $L/(c/\omega_{\rm P}) = 2000$ (see panel labels). The red dotted line in each panel shows the scaling $\propto K_{\parallel}^{-1/2}$ while the blue dotted line shows $\propto K_{\parallel}^{-3/4}$. To increase the contrast in the high- K_{\parallel} tails of these PDFs, we normalize the PDFs such that the integral over the 1D PDF of $\sqrt{|B^2/4\pi + P_{\perp} - P_{\parallel}|}$ at each K_{\parallel} is unity.

onantly scatter off of fewer field-line bends. The positive trend between $\lambda_{\rm mfp,\,curve}$ and $\overline{r_{\rm g}}$ weakens with decreasing $\delta B/B_0$, with $\delta B/B_0 \approx 1$ possibly showing a transition to a small-amplitude turbulence regime where curvature is more effective at scattering particles with larger $\overline{r_g}$. Given that $\overline{r_g}$ is proportional to a particle's energy, the trend of increasing $\lambda_{\rm mfp,\,curve}$ with increasing $\overline{r_{\rm g}}$ (for $\delta B/B_0>1$) is consistent with observations of cosmic rays in the Milky Way (A. W. Strong et al. 2007; M. Aguilar et al. 2016; E. Amato & P. Blasi 2018). In fact, our moderate- to large- $\delta B/B_0$ cases exhibit trends close to $\lambda_{\rm mfp,\,curve} \propto \overline{r_{\rm g}}^{0.3-0.5}$; this is broadly consistent with observations of Galactic cosmic rays, although it requires that a significant fraction of the Galaxy is characterized by $\delta B/B_0 \gtrsim$ a few. However, we caution that a standard mean free path may not be the most suitable metric for transport through magnetic field bends; recent high-resolution MHD simulations suggest that this transport may not be strictly diffusive, with particles exhibiting a wide distribution of scattering timescales (P. Kempski et al. 2025).

In collisionless plasmas with high β (e.g., the ICM), thermal-Larmor-scale fluctuations are believed to also play a role in scattering and confining particles. In P. Reichherzer et al. (2025), the authors show that fluctuations seeded by the mirror instability (i.e. "micromirrors") are the dominant source of cosmic ray scattering and confinement up to \sim TeV energies; beyond this transition energy, cosmic rays mainly interact with structures in the inertial range of the ambient turbu-

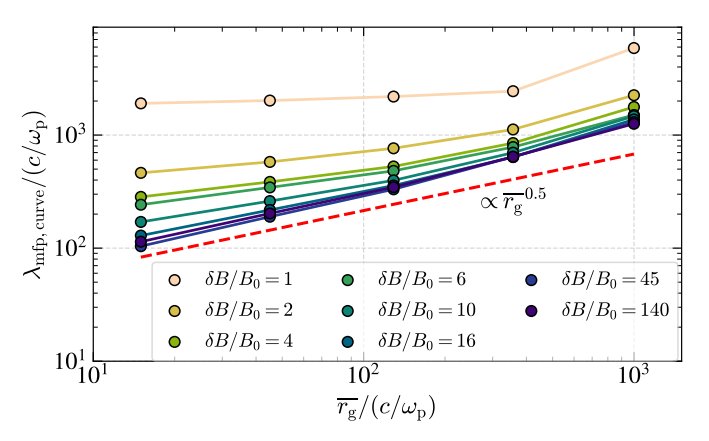


Figure 14. Mean free paths to resonant curvature scattering, $\lambda_{\rm mfp,\, curve}$ (Equation (24)), computed for $\ell/(c/\omega_{\rm p}) \sim \overline{r_{\rm g}}/(c/\omega_{\rm p}) = 15,\, 45,\, 129,\, 357,\, {\rm and}\, 999$ for each of our simulations with $L/(c/\omega_{\rm p}) = 2000$. The dashed red line indicates a scaling $\lambda_{\rm mfp,\, curve} \propto \overline{r_{\rm g}}^{0.5}$, consistent with observations of Galactic cosmic rays.

lence. While the TeV transition energy was computed assuming a 100% volume-filling fraction for the micromirrors, the authors note that this energy should be reduced by a factor of $f_{\rm mm}^{1/(2-\delta)}$ for a more realistic filling fraction, $f_{\rm mm}$, and for δ set by the specific mesoscale turbulence model (e.g., $\delta=1/3$ corresponds to an isotropic Kolmogorov-like turbulence (A. Kolmogorov 1941), while $\delta=1/2$ corresponds to Iroshnikov-Kraichnan turbulence (P. S. Iroshnikov 1964; R. H. Kraichnan 1965)). Taking $f_{\rm mm}$ to be 20% (based

on our $\delta B/B_0 \approx 140$ case with $L/(c/\omega_{\rm p})=2000)$, the TeV transition energy is only reduced by a factor of ~ 3 ; for $f_{\rm mm} \approx 4\%$ (based on our $\delta B/B_0 \approx 2$ case with $L/(c/\omega_{\rm p})=2000$), the transition energy is reduced by a factor of roughly 10. We note that our measurements of the mirror-filling fraction are upper bounds, though we do not expect them to decrease much at higher $L/(c/\omega_{\rm p})$ given that they appear to be converging with $L/(c/\omega_{\rm p})$ in Figure 11; therefore, the TeV transition energy in the ICM appears robust assuming that the scale and amplitude of the micromirrors is as estimated in P. Reichherzer et al. (2025).

6.2. Implications for particle acceleration in collisionless large-amplitude turbulence

The intermittent structures studied in this work – namely, sharp magnetic field-line bends and rapid field reversals – may allow collisionless large-amplitude turbulence to efficiently accelerate charged particles. In particular, we identify at least two mechanisms by which large-amplitude turbulence could energize particles: curvature-drift acceleration and magnetic pumping.

The broad power-law distribution in field-line curvature present in our simulations has a significant impact on curvature-drift acceleration, whereby particles following a field line can gain or lose energy while moving through regions of changing magnetic field direction in the presence of a motional electric field (J. F. Drake et al. 2006; J. T. Dahlin et al. 2014, 2017; M. Lemoine 2021; V. Bresci et al. 2022; M. Lemoine 2022, 2025). Recent work shows that curvature-drift acceleration is dominant over other drift-induced energization mechanisms, such as ∇B -drift and polarization drift, as well as betatron acceleration in magnetically-dominated turbulence (S. Sebastian & L. Comisso 2025). Following that work, we can use as a proxy for the efficacy of curvature-drift acceleration the field-line contraction,

$$\omega_{\mathbf{K}} \equiv \mathbf{K} \cdot \mathbf{v}_{\mathrm{E}},$$
 (25)

where $\mathbf{K} \equiv \hat{\mathbf{b}} \cdot \nabla \hat{\mathbf{b}}$ is the vector curvature and $\mathbf{v}_{\rm E} \equiv c(\mathbf{E} \times \mathbf{B})/B^2$ is the $\mathbf{E} \times \mathbf{B}$ drift velocity (for \mathbf{E} the electric field). If $\omega_{\mathbf{K}} > 0$, the particle will see a contracting field line as it approaches a bend and energy from the released magnetic tension will be transferred to the particle (i.e., the particle will experience a "head-on" collision); if $\omega_{\mathbf{K}} < 0$, the particle will see a stretching field line as it approaches a bend and energy will be transferred from the particle to the strengthening magnetic field (i.e., the particle will experience a "tail-on" collision).

In Figure 15, we show the 1D PDFs of field-line contraction, $\omega_{\mathbf{K}}$, for our simulations with $\delta B/B_0 \approx 1, 4, 10$

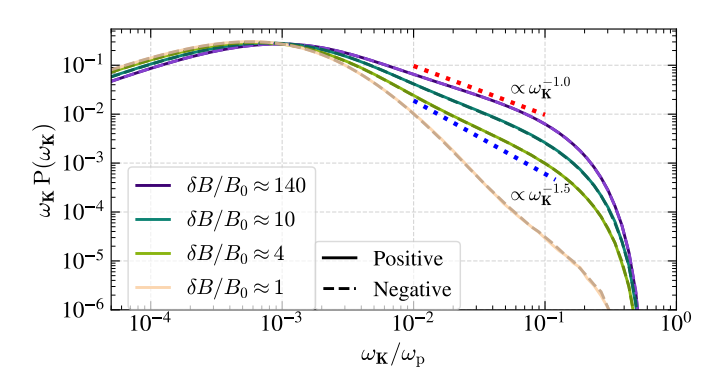


Figure 15. 1D PDFs of field-line contraction, $ω_{\mathbf{K}}$ (Equation (25)) for our simulations with $\delta B/B_0 \approx 1$, 4, 10, and 140 and $L/(c/ω_{\mathbf{p}}) = 2000$; the PDFs of positive $ω_{\mathbf{K}}$ values are shown with solid lines while the PDFs of the magnitude of negative values are shown with dashed lines. The red dotted line indicates a scaling $P(ω_{\mathbf{K}}) \propto ω_{\mathbf{K}}^{-2.0}$ (or $ω_{\mathbf{K}} P(ω_{\mathbf{K}}) \propto ω_{\mathbf{K}}^{-1.0}$) while the blue dotted line indicates a scaling $P(ω_{\mathbf{K}}) \propto ω_{\mathbf{K}}^{-1.5}$ (or $ω_{\mathbf{K}} P(ω_{\mathbf{K}}) \propto ω_{\mathbf{K}}^{-1.5}$).

and 140; since we compute these PDFs in log space, we plot separate PDFs for positive $\omega_{\mathbf{K}}$ (solid lines) and for the absolute value of negative $\omega_{\mathbf{K}}$ (dashed lines). Each PDF possesses a power-law tail at large $\omega_{\mathbf{K}}$, largely following the power-law tail at high field-line curvature; as in our 1D PDFs of K_{\parallel} , the power-law becomes steeper as $\delta B/B_0$ decreases, with the $\delta B/B_0 \approx 140$ PDF exhibiting a slope close to $P(\omega_{\mathbf{K}}) \propto P(K_{\parallel}) \propto \omega_{\mathbf{K}}^{-2.0}$ and the $\delta B/B_0 \approx 4$ PDF exhibiting a slope close to $P(\omega_{\mathbf{K}}) \propto P(K_{\parallel}) \propto \omega_{\mathbf{K}}^{-2.5}$. Additionally, the PDFs of positive and negative $\omega_{\mathbf{K}}$ practically overlap, indicating that regions of field-line relaxation and field-line stretching are equally abundant in our turbulence; regardless, net particle energization can still result from stochastic energy exchange (i.e., second-order Fermi acceleration) despite there being no persistent net contraction. Given that the acceleration rate of curvature-drift acceleration follows $\dot{\gamma}/\gamma \propto \omega_{\mathbf{K}}$, one should expect a distribution of acceleration rates that is strongly affected by intermittency, with the power-law tails in $P(\omega_{\mathbf{K}})$ indicating more efficient particle acceleration at larger $\delta B/B_0$. Evidently, curvature-drift acceleration can be highly effective in large-amplitude turbulence.

In addition to curvature-drift acceleration, scattering off thermal-Larmor-scale fluctuations, such as those seeded by the mirror and firehose instabilities, can also heat and accelerate particles. In one such channel for particle energization called magnetic pumping, particle scattering off microscale fluctuations works in concert with the turbulent flow to energize particles (J. M. Berger et al. 1958; E. Lichko et al. 2017; F. Ley et al. 2023): if the rate of scattering is comparable to the rate of bulk deformation of the plasma, an excess of energy

can be transferred from particle motions perpendicular to the local magnetic field to motions parallel to the field due to the uneven response of the parallel and perpendicular pressures to adiabatic changes in the magnetic field. In our simulated electron-positron plasmas, thermal electrons and positrons can only be heated by the Larmor-scale fluctuations they seed; however, in an electron-ion plasma with sufficient scale separation between the electron and ion Larmor radii, nonthermal electrons can be accelerated by scattering off of ion-scale waves (A. Tran et al. 2023).

One particularly promising application of particle acceleration in collisionless large-amplitude turbulence is that of fossil electron re-acceleration in galaxy clusters. Some clusters, particularly disturbed or merging clusters, emit prominent MHz-GHz radio signals due to synchrotron and inverse-Compton cooling of energetic (1-100 GeV) cosmic ray electrons (CRe) over Myr-Gyr timescales (R. J. van Weeren et al. 2019). It is widely believed that these radiating CRe were re-accelerated from a population of "fossil" electrons, lower-energy (1-100 MeV) nonthermal electrons that do not emit detectable light and can remain dormant in the ICM for gigayears due to negligible collisional losses and minimal radiative losses at MeV energies (T. A. Enßlin 1999; V. Petrosian 2001; A. Pinzke et al. 2013). The mechanism by which these fossil CRe are energized is still unclear, but the turbulence in which these CRe reside is almost certainly large-amplitude, since observations of energy equipartition in the ICM provide strong evidence of small-scale dynamo amplification (A. Bonafede et al. 2010; Hitomi Collaboration et al. 2016). Future work should quantify the relative roles of curvature-drift, magnetic pumping, and other mechanisms in accelerating fossil electrons in the ICM.

7. SUMMARY AND CONCLUSIONS

We performed fully kinetic 3D simulations of moderately subsonic, large-amplitude turbulence in a collision-less electron-positron plasma. By varying the strength of an initially weak mean magnetic field and allowing the plasma to reach a steady state under the influence of a stochastic driver, we were able to simulate steady-state turbulence with a wide range of $\delta B/B_0$, from $\delta B/B_0 \approx 1$ up to $\delta B/B_0 \approx 140$ (which resembles the initially unmagnetized $\delta B/B_0 \to \infty$ case, analyzed in detail in L. Sironi et al. (2023)); this scan in mean-field strength also yielded a range of plasma β in steady state, from $\beta \approx 1$ for $\delta B/B_0 \approx 1$ to $\beta \approx 4$ for $\delta B/B_0 \approx 140$. We also varied the scale separation between the turbulent driving scale and the kinetic scale, $L/(c/\omega_{\rm p})$, between 500, 1000, and 2000. In steady state, we analyzed the sta-

tistical properties of the intermittency in our simulated turbulence, focusing specifically on two classes of structures: sharp magnetic field-line bends (and rapid field reversals) and thermal-Larmor-scale magnetic field fluctuations (imprinted by the pressure-anisotropy-induced mirror and firehose instabilities). While we did not track individual particles or field lines in this work, our statistical analysis allowed us to infer the role of intermittent structures in both particle transport and acceleration.

The main conclusions of our study are as follows:

- While MHD predicts a scaling between magnetic field strength (B) and scalar field-line curvature (K_{\parallel}) of $B \propto K_{\parallel}^{-1/2}$, the influence of pressure anisotropy in collisionless large-amplitude turbulence yields a steeper scaling, $B \propto K_{\parallel}^{-3/4}$.
- The 1D PDF of K_{\parallel} displays an extended power-law tail for each $\delta B/B_0$ (as also seen in MHD), indicating the abundant presence of intermittent field-line bends; this tail hardens with increasing $\delta B/B_0$, exhibiting a slope $\propto K_{\parallel}^{-2.5}$ (as also seen in MHD and the solar wind) for $\delta B/B_0 \approx 4$ and a slope $\propto K_{\parallel}^{-2.0}$ for $\delta B/B_0 \approx 140$.
- The shape of the 1D PDF of the perpendicular reversal scale, K_{\perp} , differs substantially from its MHD counterpart, displaying a power-law slope for smaller $\delta B/B_0$ ($\delta B/B_0 \lesssim 10$) and an extended plateau for larger $\delta B/B_0$ ($\delta B/B_0 \gtrsim 16$).
- Pressure-anisotropy-induced mirror and firehose fluctuations are present in all of our simulations, but their volume-filling fractions decrease steadily towards smaller $\delta B/B_0$; for $\delta B/B_0 \approx 140$, roughly 20% of the volume is mirror-unstable and 6% is firehose-unstable, while for $\delta B/B_0 \approx 2$, 4% of the volume is mirror-unstable and 2% is firehose-unstable.
- Both sharp field-line bends and Larmor-scale mirror fluctuations can affect the transport of charged particles through collisionless large-amplitude turbulence. By integrating over 1D PDFs of coarse-grained field-line curvature, we find that the particle mean free path to non-adiabatic ("resonant") curvature scattering increases with particle energy (i.e., mean gyroradius) and decreases with $\delta B/B_0$; for large $\delta B/B_0$, this mean free path scales roughly with the square-root of energy.
- Sharp field-line bends can accelerate wellmagnetized particles via curvature-drift acceleration. The power-law tail of the distribution of

field-line curvature yields a power-law tail in the distribution of acceleration rates due to curvature-drift acceleration, with the slopes of both distributions closely matching.

Our investigation leaves a few avenues for future work. First, while pressure-anisotropy-induced instabilities did not significantly affect the curvature statistics in our present suite of simulations, one should investigate their impact in turbulence with higher β , where the volume-filling fractions of these fluctuations should be larger. Second, our simulations should be repeated in an electron-ion plasma, allowing for the growth of ion-Larmor-scale instabilities like ion mirror, ion firehose, and ion cyclotron. Finally, instead of extracting information about particle transport and acceleration from statistical measurements, one should self-consistently track particle and field-line trajectories through kinetic simulations of collisionless large-amplitude turbulence.

ACKNOWLEDGMENTS

We thank Yan Yang, Riddhi Bandyopadhyay, and Muni Zhou for useful discussions related to this work. R.G. was supported by NASA FINESST grant 80NSSC24K1477. L.C. was supported by NSF PHY-2308944 and NASA ATP 80NSSC24K1230. L.S. was supported by DoE Early Career Award DE-SC0023015 and NSF grant PHY2409223. P.K. was supported by NASA ATP grant 80NSSC22K0667 and the Lyman Spitzer, Jr. Fellowship at Princeton University. This research was facilitated by Multimessenger Plasma Physics Center (MPPC) NSF grants PHY2206607 and PHY2206609. The work was also supported by a grant from the Simons Foundation to L.S. (MP-SCMPS-Simulations were performed on NASA 0000147). Pleiades (GID: s2356, s2610).

Software: TRISTAN-MP (A. Spitkovsky et al. 2019)

APPENDIX

A. DEPENDENCE ON SCALE SEPARATION

In this section, we discuss the dependence on scale separation (or, equivalently, simulation box size), $L/(c/\omega_{\rm p})$, for several quantities analyzed in the main text.

Figure 16 shows the integral-scale wavenumber of the turbulent magnetic field, $k_{\rm int}$ (Equation (10)), as a function of both $\delta B/B_0$ (horizontal axis) and $L/(c/\omega_{\rm p})$ (marker shape). For each $\delta B/B_0$, increasing $L/(c/\omega_{\rm p})$ by a factor of two decreases $k_{\rm int}$ by a factor of two (i.e., increases the dominant scale of the magnetic field by a factor of two), as expected.

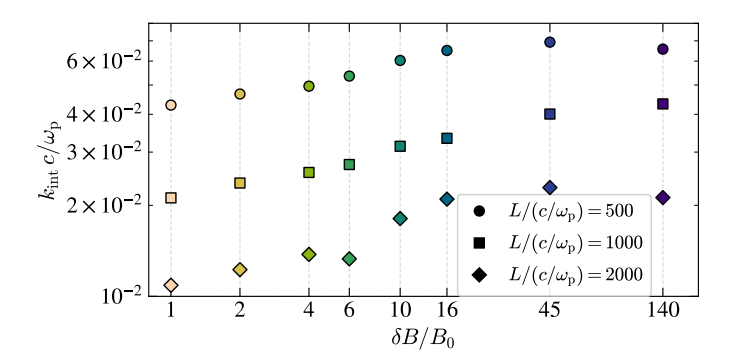


Figure 16. Integral-scale wavenumber (Equation (10)) as a function of both $\delta B/B_0$ (horizontal axis) and $L/(c/\omega_{\rm p})$ (marker shape); circles correspond to $L/(c/\omega_{\rm p})=500$, squares to $L/(c/\omega_{\rm p})=1000$, and diamonds to $L/(c/\omega_{\rm p})=2000$.

Figure 17 shows 1D PDFs of K_{\parallel} for our simulations with $\delta B/B_0 \approx 1$ (top left), 4 (top right), 10 (bottom left), and 140 (bottom right); in each panel, the dotted curve corresponds to $L/(c/\omega_{\rm p})=500$, the dashed curve to $L/(c/\omega_{\rm p})=1000$, and the solid curve to $L/(c/\omega_{\rm p})=2000$. For $\delta B/B_0\gtrsim 10$, the power-law slopes in our PDFs of K_{\parallel} are not yet converged: as we increase $L/(c/\omega_{\rm p})$, the power-law tails continually become steeper. However, for smaller $\delta B/B_0$, the power-law slopes for $L/(c/\omega_{\rm p})=1000$ and $L/(c/\omega_{\rm p})=2000$ match nicely; for $\delta B/B_0\approx 1$, we find exceptional agreement between the power-law slopes across all three box sizes.

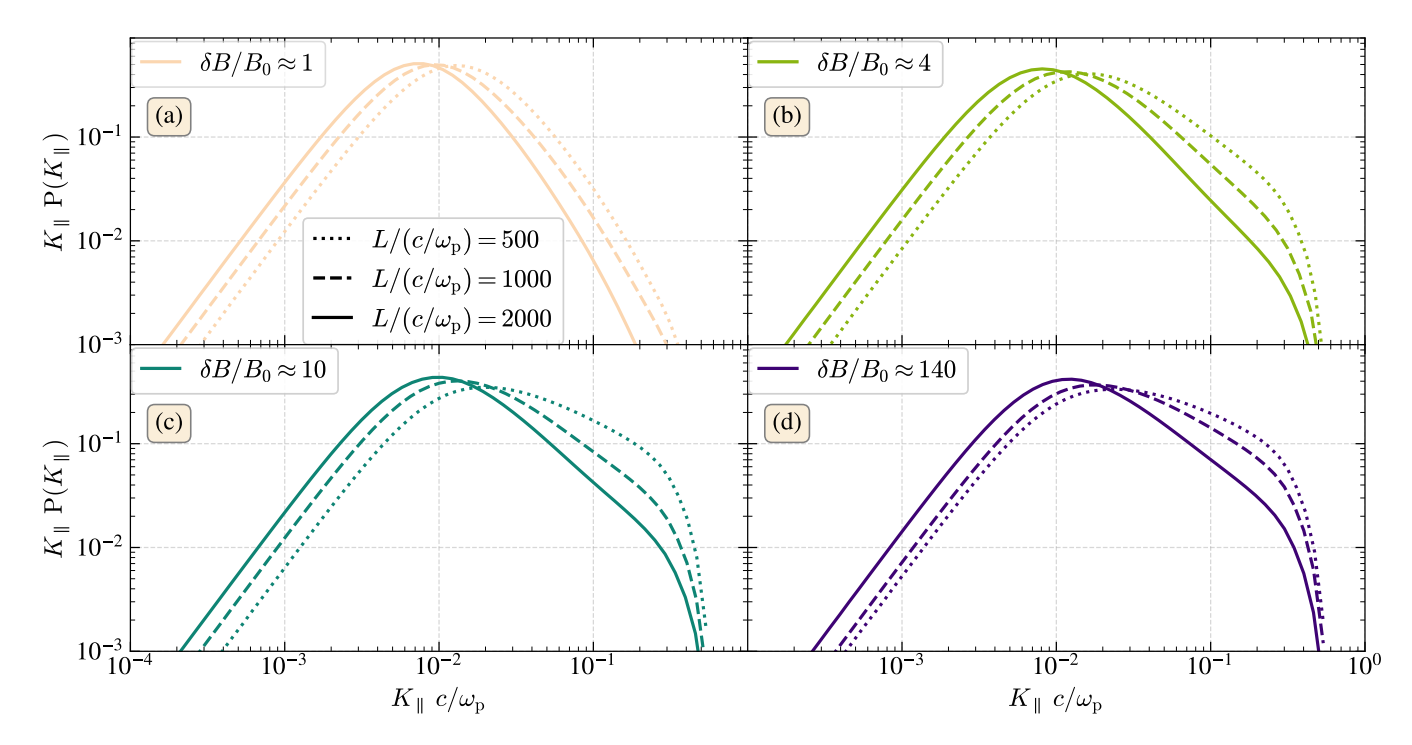


Figure 17. PDFs of K_{\parallel} as a function of $L/(c/\omega_{\rm p})$ for our simulations with $\delta B/B_0 \approx 1$ (top left), 4 (top right), 10 (bottom left), and 140 (bottom right). In each panel, the dotted curve corresponds to $L/(c/\omega_{\rm p}) = 500$, the dashed curve to $L/(c/\omega_{\rm p}) = 1000$, and the solid curve to $L/(c/\omega_{\rm p}) = 2000$.

REFERENCES

Achikanath Chirakkara, R., Seta, A., Federrath, C., & Kunz, M. W. 2024, MNRAS, 528, 937, doi: 10.1093/mnras/stad3967

Aguilar, M., Ali Cavasonza, L., Ambrosi, G., et al. 2016, PhRvL, 117, 231102,

doi: 10.1103/PhysRevLett.117.231102

Amato, E., & Blasi, P. 2018, Advances in Space Research, 62, 2731, doi: 10.1016/j.asr.2017.04.019

Arzamasskiy, L., Kunz, M. W., Squire, J., Quataert, E., & Schekochihin, A. A. 2023, Physical Review X, 13, 021014, doi: 10.1103/PhysRevX.13.021014

Balbus, S. A., & Hawley, J. F. 1998, Reviews of Modern Physics, 70, 1, doi: 10.1103/RevModPhys.70.1

 $\begin{aligned} & \text{Bale, S. D., Kasper, J. C., Howes, G. G., et al. 2009,} \\ & \text{PhRvL, } 103, \, 211101, \end{aligned}$

doi: 10.1103/PhysRevLett.103.211101

Bandyopadhyay, R., Yang, Y., Matthaeus, W. H., et al. 2020, ApJL, 893, L25, doi: 10.3847/2041-8213/ab846e

Barnes, A. 1966, The Physics of Fluids, 9, 1483, doi: 10.1063/1.1761882

Beattie, J. R., Federrath, C., Klessen, R. S., Cielo, S., & Bhattacharjee, A. 2024, arXiv e-prints, arXiv:2405.16626, doi: 10.48550/arXiv.2405.16626

Beattie, J. R., Federrath, C., Klessen, R. S., Cielo, S., & Bhattacharjee, A. 2025, Nature Astronomy, 9, 1195, doi: 10.1038/s41550-025-02551-5

Beresnyak, A. 2019, Living Reviews in Computational Astrophysics, 5, 2, doi: 10.1007/s41115-019-0005-8

Berger, J. M., Newcomb, W. A., Dawson, J. M., et al. 1958, Physics of Fluids, 1, 301, doi: 10.1063/1.1705888

Biskamp, D. 2003, Magnetohydrodynamic Turbulence Boldyrev, S. 2006, PhRvL, 96, 115002,

doi: 10.1103/PhysRevLett.96.115002

Bonafede, A., Feretti, L., Murgia, M., et al. 2010, A&A, 513, A30, doi: 10.1051/0004-6361/200913696

Boris, J. P. 1970, Proc. 4th Conf. Num. Sim. Plasmas, 3. https://apps.dtic.mil/sti/citations/ADA023511

Bresci, V., Lemoine, M., Gremillet, L., et al. 2022, PhRvD, 106, 023028, doi: 10.1103/PhysRevD.106.023028

Brunetti, G., & Lazarian, A. 2007, MNRAS, 378, 245, doi: 10.1111/j.1365-2966.2007.11771.x

Butsky, I. S., Hopkins, P. F., Kempski, P., et al. 2024, MNRAS, 528, 4245, doi: 10.1093/mnras/stae276

Chandrasekhar, S., Kaufman, A. N., & Watson, K. M. 1958, Proc. R. Soc. London A, 245, 435, doi: 10.1098/rspa.1958.0094

- Chew, G. F., Goldberger, M. L., & Low, F. E. 1956, Proceedings of the Royal Society of London Series A, 236, 112, doi: 10.1098/rspa.1956.0116
- Cho, J., & Lazarian, A. 2003, MNRAS, 345, 325, doi: 10.1046/j.1365-8711.2003.06941.x
- Comisso, L., & Sironi, L. 2018, PhRvL, 121, 255101, doi: 10.1103/PhysRevLett.121.255101
- Comisso, L., & Sironi, L. 2019, ApJ, 886, 122, doi: 10.3847/1538-4357/ab4c33
- Comisso, L., & Sironi, L. 2022, ApJL, 936, L27, doi: 10.3847/2041-8213/ac8422
- Dahlin, J. T., Drake, J. F., & Swisdak, M. 2014, Physics of Plasmas, 21, 092304, doi: 10.1063/1.4894484
- Dahlin, J. T., Drake, J. F., & Swisdak, M. 2017, Physics of Plasmas, 24, 092110, doi: 10.1063/1.4986211
- Davidson, P. A. 2015, Turbulence: An Introduction for Scientists and Engineers, 2nd edn. (Oxford: Oxford University Press, Incorporated)
- Davis, Z., Comisso, L., & Giannios, D. 2024, ApJ, 964, 14, doi: 10.3847/1538-4357/ad284c
- Dennis, T. J., & Chandran, B. D. G. 2005, ApJ, 622, 205, doi: 10.1086/427424
- Drake, J. F., Swisdak, M., Che, H., & Shay, M. A. 2006, Nature, 443, 553, doi: 10.1038/nature05116
- Enßlin, T. A. 1999, in Diffuse Thermal and Relativistic Plasma in Galaxy Clusters, ed. H. Boehringer, L. Feretti, & P. Schuecker, 275.
 - https://arxiv.org/abs/astro-ph/9906212
- Fielding, D. B., Ripperda, B., & Philippov, A. A. 2023, ApJL, 949, L5, doi: 10.3847/2041-8213/accf1f
- Galishnikova, A. K., Kunz, M. W., & Schekochihin, A. A. 2022, Physical Review X, 12, 041027, doi: 10.1103/PhysRevX.12.041027
- Gan, Z., Li, H., Fu, X., & Du, S. 2022, ApJ, 926, 222, doi: 10.3847/1538-4357/ac4d9d
- Gary, S. P. 1993, Electromagnetic temperature anisotropy instabilities in uniform plasmas, Cambridge Atmospheric and Space Science Series (Cambridge University Press), 123–142
- Goldreich, P., & Sridhar, S. 1995, ApJ, 438, 763, doi: 10.1086/175121
- Ha, T., Nättilä, J., Davelaar, J., & Sironi, L. 2025, ApJL, 985, L31, doi: 10.3847/2041-8213/add47b
- Hasegawa, A. 1969, The Physics of Fluids, 12, 2642, doi: 10.1063/1.1692407
- Haverkorn, M. 2015, in Astrophysics and Space Science
 Library, Vol. 407, Magnetic Fields in Diffuse Media, ed.
 A. Lazarian, E. M. de Gouveia Dal Pino, & C. Melioli,
 483, doi: 10.1007/978-3-662-44625-6_17

- Hitomi Collaboration, Aharonian, F., Akamatsu, H., et al. 2016, Nature, 535, 117, doi: 10.1038/nature18627
- Huang, S. Y., Zhang, J., Sahraoui, F., et al. 2020, ApJL, 898, L18, doi: 10.3847/2041-8213/aba263
- Iroshnikov, P. S. 1964, Soviet Ast., 7, 566
- Jao, C.-S., & Hau, L.-N. 2020, Phys. Rev. E, 101, 043205, doi: 10.1103/PhysRevE.101.043205
- Kempski, P., Fielding, D. B., Quataert, E., et al. 2025, arXiv e-prints, arXiv:2507.10651, doi: 10.48550/arXiv.2507.10651
- Kempski, P., Fielding, D. B., Quataert, E., et al. 2023, MNRAS, 525, 4985, doi: 10.1093/mnras/stad2609
- Kolmogorov, A. 1941, Akademiia Nauk SSSR Doklady, 30, 301
- Kraichnan, R. H. 1965, Physics of Fluids, 8, 1385, doi: 10.1063/1.1761412
- Kulsrud, R. M., Sagdeev, R. N., & Rosenbluth, M. N. 1980, MHD description of plasma: Handbook of plasma physics,
- Kunz, M. W., Jones, T. W., & Zhuravleva, I. 2022, in Handbook of X-ray and Gamma-ray Astrophysics, ed.
 C. Bambi & A. Sangangelo, 56, doi: 10.1007/978-981-16-4544-0_125-1
- Lazarian, A., Xu, S., & Hu, Y. 2023, Frontiers in Astronomy and Space Sciences, 10, 1154760, doi: 10.3389/fspas.2023.1154760
- Lemoine, M. 2021, PhRvD, 104, 063020, doi: 10.1103/PhysRevD.104.063020
- Lemoine, M. 2022, PhRvL, 129, 215101, doi: 10.1103/PhysRevLett.129.215101
- Lemoine, M. 2023, Journal of Plasma Physics, 89, 175890501, doi: 10.1017/S0022377823000946
- Lemoine, M. 2025, PhRvE, 112, 015205, doi: 10.1103/3xxg-x5dg
- Ley, F., Zweibel, E. G., Riquelme, M., et al. 2023, ApJ, 947, 89, doi: 10.3847/1538-4357/acb3b1
- Lichko, E., Egedal, J., Daughton, W., & Kasper, J. 2017, ApJL, 850, L28, doi: 10.3847/2041-8213/aa9a33
- Lübke, J., Effenberger, F., Wilbert, M., Fichtner, H., & Grauer, R. 2025, arXiv e-prints, arXiv:2509.15320, doi: 10.48550/arXiv.2509.15320
- Majeski, S., Kunz, M. W., & Squire, J. 2024, Journal of Plasma Physics, 90, 535900601, doi: 10.1017/S0022377824001296
- Maron, J., & Goldreich, P. 2001, ApJ, 554, 1175, doi: 10.1086/321413
- Matsumoto, H., & Omura, Y. 1993, https://books.google.com/books?id=BRLePAAACAAJ

- Matthaeus, W. H., Wan, M., Servidio, S., et al. 2015, Philosophical Transactions of the Royal Society of London Series A, 373, 20140154, doi: 10.1098/rsta.2014.0154
- Narayan, R., & Medvedev, M. V. 2001, ApJL, 562, L129, doi: 10.1086/338325
- Nättilä, J. 2024, Nature Communications, 15, 7026, doi: 10.1038/s41467-024-51257-1
- Parker, E. N. 1958, Phys. Rev., 109, 1874, doi: 10.1103/PhysRev.109.1874
- Petrosian, V. 2001, ApJ, 557, 560, doi: 10.1086/321557
- Pinzke, A., Oh, S. P., & Pfrommer, C. 2013, MNRAS, 435, 1061, doi: 10.1093/mnras/stt1308
- Quataert, E., & Gruzinov, A. 1999, ApJ, 520, 248, doi: 10.1086/307423
- Reichherzer, P., Bott, A. F. A., Ewart, R. J., et al. 2025, Nature Astronomy, 9, 438, doi: 10.1038/s41550-024-02442-1
- Rincon, F. 2019, Journal of Plasma Physics, 85, 205850401, doi: 10.1017/S002237781900053910.48550/arXiv.1903. 07829
- Rincon, F., Califano, F., Schekochihin, A. A., & Valentini, F. 2016, Proceedings of the National Academy of Science, 113, 3950, doi: 10.1073/pnas.1525194113
- Rincon, F., Schekochihin, A. A., & Cowley, S. C. 2015, MNRAS, 447, L45, doi: 10.1093/mnrasl/slu179
- Rosenbluth, M. N. 1956, Los Alamos Sci. Lab. Rep., LA-2030
- Schekochihin, A., Cowley, S., Maron, J., & Malyshkin, L. 2001, PhRvE, 65, 016305, doi: 10.1103/PhysRevE.65.016305
- Schekochihin, A. A. 2022, Journal of Plasma Physics, 88, 155880501, doi: 10.1017/S0022377822000721
- Schekochihin, A. A., & Cowley, S. C. 2007, in Magnetohydrodynamics: Historical Evolution and Trends, ed. S. Molokov, R. Moreau, & H. K. Moffatt, 85, doi: 10.48550/arXiv.astro-ph/0507686
- Schekochihin, A. A., Cowley, S. C., Taylor, S. F., Maron, J. L., & McWilliams, J. C. 2004, ApJ, 612, 276, doi: 10.1086/422547
- Sebastian, S., & Comisso, L. 2025, arXiv e-prints, arXiv:2510.20628, doi: 10.48550/arXiv.2510.20628
- Shakura, N. I., & Sunyaev, R. A. 1973, A&A, 24, 337
- She, Z.-S., & Leveque, E. 1994, PhRvL, 72, 336, doi: 10.1103/PhysRevLett.72.336
- Sironi, L., Comisso, L., & Golant, R. 2023, PhRvL, 131, 055201, doi: 10.1103/PhysRevLett.131.055201
- Sironi, L., & Narayan, R. 2015, ApJ, 800, 88, doi: 10.1088/0004-637X/800/2/88

- Spitkovsky, A., Gargate, L., Park, J., & Sironi, L. 2019, TRISTAN-MP: TRIdimensional STANford - Massively Parallel code,, Astrophysics Source Code Library, record ascl:1908.008 http://ascl.net/1908.008
- Squire, J., Kunz, M. W., Arzamasskiy, L., et al. 2023, Journal of Plasma Physics, 89, 905890417, doi: 10.1017/S0022377823000727
- Squire, J., Schekochihin, A. A., Quataert, E., & Kunz, M. W. 2019, Journal of Plasma Physics, 85, 905850114, doi: 10.1017/S0022377819000114
- St-Onge, D. A., & Kunz, M. W. 2018, ApJL, 863, L25, doi: 10.3847/2041-8213/aad638
- Strong, A. W., Moskalenko, I. V., & Ptuskin, V. S. 2007, Annual Review of Nuclear and Particle Science, 57, 285, doi: 10.1146/annurev.nucl.57.090506.123011
- Tran, A., Sironi, L., Ley, F., Zweibel, E. G., & Riquelme,M. A. 2023, ApJ, 948, 130,doi: 10.3847/1538-4357/acbef9
- Uhlenbeck, G. E., & Ornstein, L. S. 1930, Physical Review, 36, 823, doi: 10.1103/PhysRev.36.823
- Umeda, T., Omura, Y., Tominaga, T., & Matsumoto, H. 2003, Computer Physics Communications, 156, 73, doi: 10.1016/S0010-4655(03)00437-5
- van Weeren, R. J., de Gasperin, F., Akamatsu, H., et al. 2019, SSRv, 215, 16, doi: 10.1007/s11214-019-0584-z
- Vlahos, L., & Isliker, H. 2023, Physics of Plasmas, 30, 040502, doi: 10.1063/5.0141512
- Wan, M., Matthaeus, W. H., Karimabadi, H., et al. 2012,PhRvL, 109, 195001,doi: 10.1103/PhysRevLett.109.195001
- Yang, Y., Wan, M., Matthaeus, W. H., et al. 2019, Physics of Plasmas, 26, 072306, doi: 10.1063/1.5099360
- Yee, K. 1966, IEEE Transactions on Antennas and Propagation, 14, 302, doi: 10.1109/TAP.1966.1138693
 Zhdankin, V. 2021, ApJ, 922, 172, doi: 10.3847/1538-4357/ac222e
- Zhdankin, V., Uzdensky, D. A., Perez, J. C., & Boldyrev, S. 2013, ApJ, 771, 124, doi: 10.1088/0004-637X/771/2/124
- Zhou, M., Liu, Z., & Loureiro, N. F. 2023, MNRAS, 524, 5468, doi: 10.1093/mnras/stad2231
- Zhou, M., Zhdankin, V., Kunz, M. W., Loureiro, N. F., & Uzdensky, D. A. 2024, ApJ, 960, 12, doi: 10.3847/1538-4357/ad0b0f
- Zrake, J., & MacFadyen, A. I. 2012, ApJ, 744, 32, doi: 10.1088/0004-637X/744/1/32
- Zweibel, E. G. 2013, Physics of Plasmas, 20, 055501, doi: 10.1063/1.4807033
- Zweibel, E. G. 2017, Physics of Plasmas, 24, 055402, doi: 10.1063/1.4984017